Check for updates

New Phytologist

Research

Leaf CO_2 response curve fitting method matters: cross-tool assumptions spread photosynthetic parameters and bias leaf–canopy photosynthesis

Yingnan Wei[1], Zipiao Ye[2,3], Chongya Jiang[4], Carl J. Bernacchi[5,6], Chutao Liang[1,7], Gang Zhao[1,8], Ning Yao[9], Xinyi Fan[1], Qiang Yu[1,8] and Genghong Wu[1,8]

[1]State Key Laboratory of Soil and Water Conservation and Desertification Control, College of Soil and Water Conservation Science and Engineering, Northwest A&F University, Yangling, Shaanxi, 712100, China; [2]New Quality Productivity Research Center, Guangdong ATV College of Performing Arts, Deqing, Guangdong, 526631, China; [3]Institute of Biophysics, Math & Physics College, Jinggangshan University, Ji'an, Jiangxi, 343009, China; [4]National Engineering and Technology Center for Information Agriculture (NETCIA), MARA Key Laboratory of Crop System Analysis and Decision Making, MOE, Engineering Research Center of Smart Agriculture, Jiangsu Key Laboratory for Information Agriculture, Institute of Smart Agriculture, Nanjing Agricultural University, Nanjing, Jiangsu, 210095, China; [5]Agroecosystem Sustainability Center, Institute for Sustainability, Energy, and Environment, University of Illinois at Urbana-Champaign, Urbana, IL 61801, USA; [6]Department of Plant Biology, University of Illinois at Urbana-Champaign, Urbana, IL 61801, USA; [7]College of Environmental Science and Engineering, Shanxi Institute of Science and Technology, Jincheng, Shanxi, 048000, China; [8]Institute of Soil and Water Conservation, Chinese Academy of Sciences and Ministry of Water Resources, Yangling, Shaanxi, 712100, China; [9]College of Water Resources and Architectural Engineering/Key Lab of Agricultural Water and Soil Engineering of Education Ministry, Northwest A&F University, Yangling, Shaanxi, 712100, China

Author for correspondence:
Genghong Wu
Email: wugh@nwafu.edu.cn

Received: *13 April 2026*
Accepted: *29 May 2026*

New Phytologist (2026)
doi: 10.1111/nph.71358

Key words: C_3 crops, fitting configuration, J_{25}, leaf CO_2 response (A_n–C_i) curve, leaf–canopy photosynthesis simulation, SCOPE, $V_{cmax,25}$.

Summary

- A_n–C_i curves are used to infer $V_{cmax,25}$ and J_{25} for terrestrial biosphere models, but fitting-tool assumptions can alter both parameters; although $V_{cmax,25}$ varies more, J_{25} differences can also shift inferred limitation regimes and thereby affect propagation from leaf to canopy simulations.
- We compared 11 widely used A_n–C_i fitting configurations and one optimal model configuration across four C_3 crops (soybean, perennial ryegrass, red clover, and winter wheat), ran two complementary sensitivities (one-at-a-time toggles relative to a baseline and variance-based decomposition), and used the resulting parameters in the Soil-Canopy Observation, Photochemistry and Energy (SCOPE) model to simulate A_n and gross primary productivity (GPP).
- $V_{cmax,25}$ differed by up to fourfold across tools, with consistent fingerprints across crops. Pooled sensitivities identified mesophyll conductance (g_m) and limiting-rate selection as the dominant drivers of between-tool spread. In SCOPE, using the same assumptions in simulation as in parameter estimation kept leaf A_n errors below 9%, while mismatched assumptions produced A_n deviations −68% to +81% across crops and soybean GPP shifts −12% to +20%.
- $V_{cmax,25}$ is transportable only with its assumptions. Users should align g_m, limiting-rate, and kinetic settings with intended simulations or treat catalogued values as priors unless recomputed from raw A_n–C_i data.

Introduction

Photosynthesis is a foundational biological process that underpins terrestrial carbon uptake and is central to research in plant physiology, ecosystem ecology, and crop science, where photosynthetic traits are used to interpret leaf-level processes, trait coordination, and responses to environmental variability (Wan & Ma, 2024; Yu *et al.*, 2024). At broader scales, it governs gross primary production (GPP), the dominant land–atmosphere carbon flux shaping carbon–climate feedbacks (Campbell *et al.*, 2017; Hu *et al.*, 2021) and supporting a major terrestrial carbon sink (Keenan & Williams, 2018; Luo *et al.*, 2019). Despite decades of model development, global GPP estimates from terrestrial biosphere models (TBMs) remain highly uncertain, ranging from roughly 90–170 Pg C yr^{-1} (Zheng *et al.*, 2020). One important source of this uncertainty is the specification and constraint of photosynthetic capacity, which provides a key biochemical upper bound of carbon uptake.

The Farquhar–von Caemmerer–Berry (FvCB) biochemical model (Farquhar *et al.*, 1980; von Caemmerer, 2000) is widely used to estimate leaf photosynthetic capacity from gas-exchange data, with capacity commonly summarized by parameters

© 2026 The Author(s).
New Phytologist © 2026 New Phytologist Foundation.

standardized to 25°C, including the maximum Rubisco carboxylation capacity ($V_{cmax,25}$) and electron-transport capacity (J_{25}). These parameters are widely used as both model inputs and physiological traits for cross-study synthesis, and their robust and comparable estimation is essential for leaf-level physiology and large-scale carbon modeling. Inaccurate specification of $V_{cmax,25}$ has been shown to induce substantial biases in simulated photosynthesis and to contribute importantly to GPP uncertainty in modeling studies (Bonan *et al.*, 2011; Walker *et al.*, 2017; Xu *et al.*, 2024), highlighting the importance of accurately estimating key photosynthetic parameters.

To constrain $V_{cmax,25}$ across leaf to global scales, diverse approaches have been developed. Statistical approaches rely on empirical relationships between field measurements and plant traits or remotely sensed proxies, including leaf nitrogen or Chl content (Walker *et al.*, 2014; Luo *et al.*, 2019; Lu *et al.*, 2022), vegetation indices (Lu *et al.*, 2025), and hyperspectral reflectance (Sexton *et al.*, 2021; Wan & Ma, 2024). Inversion approaches retrieve effective $V_{cmax,25}$ by assimilating flux-tower GPP (Qian *et al.*, 2021) or satellite-derived solar-induced Chl fluorescence (SIF) into TBMs (He *et al.*, 2019; Liu *et al.*, 2023). Mechanistic approaches grounded in optimality theory infer $V_{cmax,25}$ from principles of nitrogen allocation and coordination among carboxylation, electron transport, and water costs (Smith *et al.*, 2019; Detto & Xu, 2020). Although these methods extend photosynthetic capacity estimation beyond the leaf scale, they often rely on leaf CO_2 response (A_n–C_i) curve fitting for calibration, benchmarking, or evaluation (Sharkey *et al.*, 2007; De Kauwe *et al.*, 2016).

The leaf A_n–C_i curve describes the response of net assimilation (A_n) to intercellular CO_2 concentration (C_i). By fitting this curve, photosynthetic capacity parameters, such as $V_{cmax,25}$ and J_{25} under saturating light, can be inferred (Farquhar *et al.*, 1980; Sharkey *et al.*, 2007). Because A_n–C_i curves are not necessarily measured at 25°C, parameters are standardized using temperature-response functions. $V_{cmax,25}$ and J_{25} jointly control Rubisco- and electron-transport–limited photosynthesis within the FvCB framework, making A_n–C_i fitting a widely used pathway for estimating key photosynthetic traits. In terrestrial biosphere and ecosystem models, empirical or structural relationships between $V_{cmax,25}$ and J_{25} are often imposed to constrain photosynthetic capacity and ensure realistic transitions between Rubisco and electron-transport limitation (Wullschleger, 1993). Therefore, beyond comparing how fitting methods alter the marginal estimates of $V_{cmax,25}$ and J_{25}, it is necessary to test whether method choice alters their coordination, including slope, ratio, and dispersion. Such method-induced differences, even when based on the same leaf-level observations, may lead to different model constraints and scale-dependent interpretations.

Over the past two decades, numerous tools have been developed to fit A_n–C_i curves and retrieve photosynthetic parameters (e.g. Sharkey *et al.*, 2007; Patrick *et al.*, 2009; Lochocki *et al.*, 2025). Early spreadsheet-based calculators such as the Long & Bernacchi (2003), Ethier & Livingston (2004), and Sharkey *et al.* (2007) tools remain widely used because of their accessibility, while more recent R packages – such as plantecophys (Duursma, 2015), photosynthesis (Stinziano *et al.*, 2021), msuRACiFit (Gregory *et al.*, 2021), and PhotoGEA (Lochocki *et al.*, 2025) – have automated limitation assignment and expanded parameterization options. Croft *et al.* (2017) used the Ethier & Livingston (2004) calculator to derive reference V_{cmax} under growing-season temperature for developing leaf Chl content–based upscaling methods, whereas Jiang *et al.* (2020) validated an optimality-based framework against $V_{cmax,25}$ derived using the Bernacchi *et al.* (2001) approach.

However, these tools are far from interchangeable. Although they are applied to the same type of data, they differ in fundamental assumptions and implementations. Key methodological choices include whether mesophyll conductance (g_m) is assumed infinite (Collatz *et al.*, 1991; Duursma, 2015) or explicitly estimated (Ethier & Livingston, 2004; Moualeu-Ngangue *et al.*, 2017), how day respiration (R_d) is constrained, whether triose phosphate utilization (TPU) limitation is considered, how the CO_2 compensation point (Γ*) in the absence of R_d is parameterized, how temperature responses are formulated, and how transitions between limiting processes are defined. As a result, identical datasets may yield divergent estimates of $V_{cmax,25}$ and J_{25} across tools, yet systematic cross-tool comparisons remain limited. More importantly, it is unclear how such discrepancies affect parameter coordination, interpretation and transferability, and their propagation in downstream leaf-, canopy-, or ecosystem-scale simulations.

Here, we address this gap by systematically evaluating 11 widely used A_n–C_i fitting tools that differ in process representation and parameterization across four C_3 crops. We first quantify how tool-specific assumptions affect estimates of $V_{cmax,25}$ and J_{25}, as well as their inferred coordination. We then propagate these parameter sets into the Soil Canopy Observation, Photochemistry and Energy fluxes (SCOPE) model (van der Tol *et al.*, 2009; Yang *et al.*, 2021), a widely used radiative transfer and energy balance framework for simulating ecosystem carbon fluxes. Within SCOPE, $V_{cmax,25}$ serves as a critical biochemical input for leaf and canopy photosynthesis. By linking parameter estimation to forward simulations of A_n and GPP, our study provides an evidence-based assessment of how methodological differences in A_n–C_i fitting affect photosynthetic capacity estimates and their downstream interpretation across scales, and offers practical guidance for improving consistency between fitting tools and model implementation in plant physiology, remote sensing, and earth system modeling.

Materials and Methods

Leaf gas exchange and Chl fluorescence measurements

Leaf gas-exchange measurements were conducted for four crops – soybean (*Glycine max* (L.) Merr), perennial ryegrass (*Lolium perenne* L.), red clover (*Trifolium pratense* L.), and winter wheat (*Triticum aestivum* L.; winter type)—under rainfed field conditions at four field sites (Table 1). Soybean data were collected

© 2026 The Author(s).
New Phytologist © 2026 New Phytologist Foundation.

14698137, 0, Downloaded from https://nph.onlinelibrary.wiley.com/doi/10.1111/nph.71358 by Northwest Agri & Forestry, Wiley Online Library on [14/06/2026]. See the Terms and Conditions (https://onlinelibrary.wiley.com/terms-and-conditions) on Wiley Online Library for rules of use; OA articles are governed by the applicable Creative Commons License

14698137, 0, Downloaded from https://nph.onlinelibrary.wiley.com/doi/10.1111/nph.71358 by Northwest Agri & Forestry, Wiley Online Library on [14/06/2026]. See the Terms and Conditions (https://onlinelibrary.wiley.com/terms-and-conditions) on Wiley Online Library for rules of use; OA articles are governed by the applicable Creative Commons License

Table 1 Field sites, sampling dates, and crop types for leaf gas-exchange measurements.

Site	Latitude	Longitude	Sampling date(s)	Crop type(s)
University of Illinois Energy Farm, USA	40.06°N	88.19°W	9 June–10 October 2019	Soybean (*Glycine max*)
Reifsteck Farm, University of Illinois, USA	39.88°N	88.15°W	9 June–3 October 2020	Soybean (*Glycine max* (L.) Merr.)
Yucheng Experimental Station, China	36.93°N	116.63°E	Winter wheat, 25 April 2023; Perennial ryegrass, 29 April 2023; Red clover, 1 May 2023	Winter wheat (*Triticum aestivum* L.); Perennial ryegrass (*Lolium perenne* L.); Red clover (*Trifolium pratense* L.)
Caoxinzhang Experimental Farm (NWAFU), Yangling, China	34.31°N	108.09°E	23 March 2025	Winter wheat (*Triticum aestivum* L., winter type)

over two consecutive years in Illinois, USA: throughout the growing season (June–October) in 2019 at the University of Illinois Energy Farm (40.06°N, 88.19°W) and over the same period in 2020 at the University of Illinois Reifsteck Farm (39.88°N, 88.15°W). Single-day measurements of perennial ryegrass and red clover were obtained between April and May 2023 at the Yucheng Experimental Station, Yucheng, China (36.93°N, 116.63°E; Ye *et al.*, 2025). Winter wheat measurements were collected at two site–year combinations: Yucheng Experimental Station, China (25 April 2023; 36.93°N, 116.63°E; Ye *et al.*, 2025), and the Caoxinzhang Experimental Farm, Northwest A&F University, Yangling, China (23 March 2025; 34.31°N, 108.09°E). Although both winter wheat datasets represent *T. aestivum* (winter type), they were collected at different sites and years and were therefore treated as two independent site–year datasets in all cross-tool comparisons.

Leaf gas exchange was measured using a portable photosynthesis system (LI-6800; Li-Cor Biosciences, Lincoln, NE, USA) at a constant flow rate of 500 μmol s^{-1} and controlled chamber humidity (40–65%). The saturating photosynthetic photon flux density (PPFD) used for A_n–C_i measurements was determined from A_n–Q (light-response) curves to ensure nonlight-limiting conditions. For each crop, A_n–C_i response curves were generated by stepwise variation of the reference CO_2 concentration (C_a) under the dataset-specific saturating PPFD (1200–2200 μmol m^{-2} s^{-1}), controlled leaf temperature (25–30°C), and stable relative humidity (40–65%). Before each curve, leaves were acclimated for 5–20 min until A_n and stomatal conductance stabilized. Detailed C_a step sequences and PPFD protocols for both A_n–C_i and A_n–Q measurements are provided in Supporting Information Table S1, and the numbers of independent biological replicates for each species, dataset, and date are reported in Table S2. Full protocols and instrument settings for A_n–C_i, A_n–Q, and simultaneous Chl fluorescence measurements (electron-transport rate, ETR, estimation) are provided in Methods S1.

FvCB framework and method configurations

The FvCB model (Farquhar *et al.*, 1980) provides the standard biochemical representation of C_3 photosynthesis and has been extensively incorporated into TBMs (Rogers, 2014; van Diepen *et al.*, 2022). In this framework, A_n is determined by the most limiting of three potential processes: Rubisco-limited carboxylation (A_c), RuBP-regeneration-limited (A_j), and TPU-limited (A_p):

$$A_n = \min\{A_c, A_j, A_p\} \quad \text{Eqn 1}$$

Rubisco-limited:

$$A_c = \frac{V_{cmax}(C_c - \Gamma^*)}{C_c + K_c(1 + O/K_o)} - R_d \quad \text{Eqn 2}$$

RuBP-regeneration-limited:

$$A_j = \frac{J(C_c - \Gamma^*)}{4C_c + 8\Gamma^*} - R_d \quad \text{Eqn 3}$$

TPU-limited:

$$A_p = 3\text{TPU} - R_d \quad \text{Eqn 4}$$

where C_c is the chloroplast CO_2 concentration, K_c and K_o are the Michaelis–Menten constants of Rubisco for CO_2 and O_2, respectively, O is O_2 concentration, J denotes the electron-transport rate. In earlier studies, this quantity was often reported as J_{max} when inferred from A_n–C_i curves measured under high light. However, following Buckley & Diaz-Espejo (2015), we distinguish it from the asymptotic J_{max} of the light-response function and refer to it here as J.

In this study, 11 widely used implementations of the FvCB framework were selected for comparison: Collatz_1991 (Collatz *et al.*, 1991), Long & Bernacchi_2003 (Long & Bernacchi, 2003), Ellsworth_2004 (Ellsworth *et al.*, 2004), Ethier & Livingston_2004 (Ethier & Livingston, 2004), Patrick_2009 (Patrick *et al.*, 2009), Sharkey_2007 (Sharkey *et al.*, 2007), Duursma_2015 (Duursma, 2015), Sharkey_2016 (2.0R; Sharkey, 2016), Moualeu-Ngangue_2017 (Moualeu-Ngangue *et al.*, 2017), Gregory_2021 (Gregory *et al.*, 2021), and Stinziano_2021 (Stinziano *et al.*, 2021). Most of these methods are deterministic curve-fitting tools that primarily return point estimates, whereas Patrick_2009 uses a hierarchical Bayesian approach that jointly estimates photosynthetic parameters and their posterior uncertainties by combining prior information with observations. We also included the optimality-based Smith_2019 approach (Smith *et al.*, 2019) as an external benchmark. Because it predicts environmentally optimal

© 2026 The Author(s).
New Phytologist © 2026 New Phytologist Foundation.

photosynthetic parameters from meteorological forcing rather than fitting A_n–C_i curves directly, it was treated separately from the Table 2 fitting configurations and is described in Estimation of $V_{cmax,25}$ and J_{25} section.

Most fitting methods were originally developed as Excel-based tools, with three later implemented as widely used R packages: *plantecophys* (Duursma_2015), *photosynthesis* (Stinziano_2021), and *msuRACiFit* (Gregory_2021). Across the 11 fitting configurations, methodological differences arise mainly from the treatment of six process variables (g_m, R_d, Γ*, $k(T)$, TPU, and limiting-rate selection) and three kinetic parameters (K_c, K_o, and Γ* at 25°C, hereafter $K_{c,25}$, $K_{o,25}$, and Γ^*_{25}, respectively), as summarized in Table 2. Some tools allow user-defined process settings; unless otherwise stated, we used the published or default configuration summarized in Table 2.

The treatment of g_m differed substantially among fitting methods. Collatz_1991, Long & Bernacchi_2003, Ellsworth_2004, Duursma_2015, and Stinziano_2021 implicitly assumed infinite g_m ($g_m = \infty$, $C_i = C_c$). By contrast, Ethier & Livingston_2004, Gregory_2021, Sharkey_2007, and Sharkey_2016 (2.0R) estimated g_m from gas-exchange data alone (Eqn 5a), whereas Moualeu-Ngangue_2017 further constrained g_m by combining gas exchange with Chl fluorescence (Eqn 5b):

$$g_m = \begin{cases} A_n/(C_i - C_c) & \text{(a)} \\ \dfrac{A_n(\alpha\beta I_{inc}\Phi_{PSII} - 4(A_n + R_d))}{\alpha\beta I_{inc}\Phi_{PSII}(C_i - \Gamma^*) - 4(C_i + 2\Gamma^*)(A_n + R_d)} & \text{(b)} \end{cases}$$

Eqn 5

where α is the fraction of incoming light absorbed by the photosystems, β is the partitioning factor of absorbed photons between PSI and PSII, I_{inc} is incident PPFD, and Φ_{PSII} is the effective quantum yield. The values of α and β are provided in Table S3.

Estimation of R_d also varied. In Long & Bernacchi_2003, Ellsworth_2004, and Stinziano_2021, R_d was fitted linearly from the low-C_i portion of the A_n–C_i curve, whereas most other methods solved R_d jointly with V_{cmax} using a nonlinear fitting. Collatz_1991 prescribed R_d as a constant fraction of V_{cmax} (Eqn 6a). Ethier & Livingston_2004 used nonlinear least-squares fitting to estimate $V_{cmax} - R_d$ and then solved for R_d (Eqn 6b):

$$R_d = \begin{cases} 0.015 \times V_{cmax} & \text{(a)} \\ x \cdot K_o \cdot \dfrac{S_{c/o} \cdot \Gamma - 0.5O}{O \cdot S_{c/o} \cdot K_c + S_{c/o} \cdot K_o \cdot K_c + 0.5O \cdot K_o} & \text{(b)} \end{cases}$$

Eqn 6

where $x = V_{cmax} - R_d$, $S_{c/o}$ is the Rubisco CO_2/O_2 specificity factor, and Γ is CO_2 compensation point derived from a nonrectangular hyperbolic fit to the A_n–C_i curve.

The treatment of Γ* varied among methods. Most methods used an Arrhenius-type response (Eqn 7a), whereas Collatz_1991 derived Γ* from Rubisco specificity (Eqn 7b). Ellsworth_2004 applied a quadratic response (Eqn 7c), and Ethier & Livingston_2004 used an alternative Arrhenius-type formulation (Eqn 7d). In Gregory_2021, $\Gamma^* = 3.52$ Pa:

$$\Gamma^* = \begin{cases} \exp\left[c - \dfrac{\Delta H_a}{R(T + 273.15)}\right] & \text{(a)} \\ O/2S_{c/o} & \text{(b)} \\ \Gamma^*_{25} + 0.2268 \cdot (T - 25) + 0.00463 \cdot (T - 25)^2 & \text{(c)} \\ \Gamma^*_{25} \cdot \exp\left[\Delta H_a(T - 25)/298.15R(T + 273.15)\right] & \text{(d)} \end{cases}$$

Eqn 7

where R is the universal gas constant; T is leaf temperature, °C; c is a dimensionless scaling constant; ΔH_a denotes activation energy.

The temperature-response function, $k(T)$, used to normalize V_{cmax} and J at measurement temperature to $V_{cmax,25}$ and J_{25}, was usually represented by the Arrhenius formulation (Eqn 8a). By contrast, Collatz_1991 employed a Q_{10}-based function with a high-temperature inhibition term (Eqn 8b), whereas Patrick_2009 and Smith_2019 adopted a peaked Arrhenius formulation (Eqn 8c):

$$k(T) = \begin{cases} \exp\left[c - \dfrac{\Delta H_a}{R \cdot (T + 273.15)}\right] & \text{(a)} \\ k_{25} \cdot Q_{10}^{(T-25)/10}\left\{1 + \exp\left[\frac{-a + b(T+273)}{R(T+273)}\right]\right\}^{-1} & \text{(b)} \\ k_{25} \cdot \exp\left[\dfrac{\Delta H_a(T - 25)}{298R(T + 273.15)}\right] \cdot \dfrac{1 + \exp\left[\frac{298 \cdot \Delta S - H_d}{298R}\right]}{1 + \exp\left[\frac{(T + 273.15) \cdot \Delta S - H_d}{R \cdot (T + 273.15)}\right]} & \text{(c)} \end{cases}$$

Eqn 8

Although Eqn (8a) has the same form as Eqn (7a), the parameter values differ because Eqn (7a) describes Γ*, whereas Eqn (8a) describes the temperature responses of V_{cmax} and J, k_{25} is the parameter value at 25°C, Q_{10} is the temperature-sensitivity coefficient, a and b are empirical constants, ΔS is an entropy term, H_d is the deactivation energy. All parameter values are provided in Table S3.

© 2026 The Author(s).
New Phytologist © 2026 New Phytologist Foundation.

14698137, 0, Downloaded from https://nph.onlinelibrary.wiley.com/doi/10.1111/nph.71358 by Northwest Agri & Forestry, Wiley Online Library on [14/06/2026]. See the Terms and Conditions (https://onlinelibrary.wiley.com/terms-and-conditions) on Wiley Online Library for rules of use; OA articles are governed by the applicable Creative Commons License

Table 2 Comparison of 11 fitting configurations used to estimate $V_{cmax,25}$ and J_{25} within the FvCB framework. Methods differ in the treatment of six processes (g_m, R_d, Γ^*, $k(T)$, TPU limitation, and limiting-rate selection) and three kinetic parameters ($K_{c,25}$, $K_{o,25}$, and Γ^*_{25}). The corresponding formulations are given in Eqns 5–8.

Method	g_m	R_d	TPU	Γ^*	$k(T)$	Limiting-rate selection	Parameters
Long & Bernacchi_2003	∞	Linear fitting	N	Eqn 7(a)	Eqn 8(a)	Full curve	$K_{c,25} = 40.4$, $K_{o,25} = 27.8$, $\Gamma^*_{25} = 4.275$
Collatz_1991	∞	Eqn 6(a)	N	Eqn 7(b)	Eqn 8(b)	Quadratic smoothing function	$K_{c,25} = 30$, $K_{o,25} = 30$, $\Gamma^*_{25} = 4.02$
Duursma_2015	∞	Nonlinear fitting	N	Eqn 7(a)	V_{cmax}: Eqn 8(a); J: Eqn 8(c)	Full curve	$K_{c,25} = 40.4$, $K_{o,25} = 27.8$, $\Gamma^*_{25} = 4.275$
Ellsworth_2004	∞	Linear fitting ($C_i < 230$)	N	Eqn 7(c)	Eqn 8(a)	A_c: $C_i < 230$, A_j: $C_i > 280$	$K_{c,25} = 40.4$, $K_{o,25} = 27.8$, $\Gamma^*_{25} = 4.275$
Ethier & Livingston_2004	Eqn 5(a)	Eqn 6(b)	N	Eqn 7(d)	Eqn 8(a)	Full curve	$K_{c,25} = 27.4$, $K_{o,25} = 41.829$, $\Gamma^*_{25} = 4.51$
Gregory_2021	Eqn 5(a)	Nonlinear fitting	Y	Fixed	Eqn 8(a)	Full curve	$K_{c,25} = 27.24$, $K_{o,25} = 16.58$, $\Gamma^*_{25} = 3.52$
Moualeu-Ngangue_2017	Eqn 5(b)	Nonlinear fitting	N	Eqn 7(a)	Eqn 8(a)	Full curve	$K_{c,25} = 27.24$, $K_{o,25} = 16.58$, $\Gamma^*_{25} = 3.74$
Patrick_2009	Bayesian estimation	Bayesian estimation	N	Bayesian estimation	Eqn 8(c)	Bayesian estimation	Bayesian estimation
Sharkey_2007	Eqn 5(a)	Nonlinear fitting	Y	Eqn 7(a)	Eqn 8(a)	A_c: $C_i < 200$, A_j: $C_i > 300$, A_p: the largest point of C_i	$K_{c,25} = 27.24$, $K_{o,25} = 16.58$, $\Gamma^*_{25} = 3.74$
Sharkey_2016 (2.0R)	Eqn 5(a)	Nonlinear fitting	Y	Eqn 7(a)	Eqn 8(a)	A_c: $C_i < 200$, A_j: $C_i > 300$, A_p: the largest point of C_i	$K_{c,25} = 27.24$, $K_{o,25} = 16.58$, $\Gamma^*_{25} = 3.74$
Stinziano_2021	∞	Linear fitting	Y	Eqn 7(a)	Eqn 8(a)	Full curve	$K_{c,25} = 40.4$, $K_{o,25} = 27.8$, $\Gamma^*_{25} = 4.275$

C_i is the intercellular CO_2 concentration; Γ^* is CO_2 compensation point without dark respiration; R_d is day respiration; TPU is Triose phosphate utilization rate; g_m is mesophyll conductance; $k(T)$ is the temperature-response function, which normalizes V_{cmax} and J at measured leaf temperature to $V_{cmax,25}$ and J_{25}; $K_{c,25}$ is Michaelis–Menten constant of Rubisco for CO_2 at 25°C; $K_{o,25}$ is Michaelis–Menten constant of Rubisco for O_2 at 25°C; Γ^*_{25} is CO_2 compensation point without dark respiration at 25°C. For Duursma_2015 and Gregory_2021, the TPU setting shown here corresponds to the default configuration used in the main-text intercomparison. In Long & Bernacchi_2003, V_{cmax} is obtained by progressively removing high-C_i points until the low-C_i region becomes approximately linear. In our dataset, this criterion was satisfied for $C_i < 200$ μmol mol^{-1}, which produced a strong linear fit ($R^2 \geq 0.85$, RMSE ≤ 3.9 μmol m^{-2} s^{-1}); this range was therefore used for V_{cmax} fitting.

© 2026 The Author(s).
New Phytologist © 2026 New Phytologist Foundation.

14698137, 0, Downloaded from https://nph.onlinelibrary.wiley.com/doi/10.1111/nph.71358 by Northwest Agri & Forestry, Wiley Online Library on [14/06/2026]. See the Terms and Conditions (https://onlinelibrary.wiley.com/terms-and-conditions) on Wiley Online Library for rules of use; OA articles are governed by the applicable Creative Commons License

14698137, 0, Downloaded from https://nph.onlinelibrary.wiley.com/doi/10.1111/nph.71358 by Northwest Agri & Forestry, Wiley Online Library on [14/06/2026]. See the Terms and Conditions (https://onlinelibrary.wiley.com/terms-and-conditions) on Wiley Online Library for rules of use; OA articles are governed by the applicable Creative Commons License

TPU limitation was either excluded (e.g. Ellsworth_2004, Ethier & Livingston_2004) or explicitly included (e.g. Sharkey_2007). It is worth noting that both Duursma_2015 and Gregory_2021 can be implemented with or without TPU. We tested both configurations and found that the differences in fitted $V_{cmax,25}$ and J_{25} were generally small (Figs S1, S2). Therefore, the main-text intercomparison used the default configuration of each method, that is TPU excluded for Duursma_2015 and TPU included for Gregory_2021.

Limiting-rate selection also differed substantially across methods. Long & Bernacchi_2003, Duursma_2015, Ethier & Livingston_2004, Gregory_2021, Moualeu-Ngangue_2017, and Stinziano_2021 used full-curve fitting. The Long & Bernacchi_2003 method estimates V_{cmax} from the low-C_i portion of the A_n–C_i curve after progressively removing higher-C_i observations. Because the original procedure does not define a universal numerical criterion for selecting the low-C_i linear region, we implemented an explicit operational rule. Candidate low-C_i ranges were evaluated using the linearized Rubisco-limited relationship, and the retained range was required to satisfy the coefficient of determination (R^2) ≥ 0.85 and root mean square error (RMSE) ≤ 3.9 μmol m^{-2} s^{-1} for the linearized fit while retaining sufficient points for stable fitting. In our dataset, $C_i < 200$ μmol mol^{-1} was the common range that met these criteria; this threshold was therefore used for the Long & Bernacchi_2003 V_{cmax} estimates. Collatz_1991 applied a quadratic smoothing function to avoid abrupt switching between adjacent limitation states. Ellsworth_2004, Sharkey_2007, and Sharkey_2016 (2.0R) separated Rubisco- and RuBP-regeneration-limited regions using fixed C_i thresholds. Patrick_2009 treated limiting-rate selection probabilistically within the Bayesian framework rather than imposing deterministic thresholds.

In addition to these process-level differences, the methods also differed in their treatment of kinetic constants. Most methods did not estimate $K_{c,25}$, $K_{o,25}$, or Γ^*_{25} from the A_n–C_i data, but instead prescribed method-specific fixed values (Table 2). Across configurations, $K_{c,25}$ ranged from 27.24 to 40.4 Pa, $K_{o,25}$ from 16.58 to 41.829 kPa, and Γ^*_{25} from 3.52 to 4.51 Pa. Patrick_2009 did not rely on a single fixed parameter set, but instead estimated parameters and their uncertainty within a hierarchical Bayesian framework.

Estimation of $V_{cmax,25}$ and J_{25}

Except for methods originally implemented in dedicated R packages, all 11 methods A_n–C_i fitting tools summarized in Table 2 were reproduced within a unified Python workflow to ensure consistent data handling and parameter retrieval. For each A_n–C_i curve, we estimated parameters ($V_{cmax,25}$, J_{25}, and where available R_d, g_m, and Γ*) and applied a quality-control filter to exclude nonconverged or clearly poor fits that fail to reproduce the observed curve shape, using standard goodness-of-fit metrics (R^2 and RMSE; Sharkey *et al.*, 2007; Stinziano *et al.*, 2021). Specifically, individual-curve fits were retained only if $R^2 \geq 0.85$ and RMSE ≤ 6.3 μmol m^{-2} s^{-1}. These criteria were used to identify nonconverged or clearly poor fits that failed to reproduce the observed A_n–C_i curve shape, while retaining natural measurement noise and leaf-to-leaf variability. Under this standard, curve retention rates remained very high across methods (98–100%; Table S4), thereby limiting method-specific retention bias in the cross-method comparisons. Species × date summaries were included only when ≥ 3 biological replicates were retained after quality-control. The resulting R^2 and RMSE distributions are shown in Fig. S3 (soybean) and Fig. S4 (other crops).

Because negative R_d is physiologically implausible, we applied a two-pass non-negativity correction: each curve was first fitted under the native assumptions of the configuration; if $R_d < 0$, we fixed $R_d = 0$ and recalculated the remaining parameters. This correction occurred mainly in Long & Bernacchi_2003, Duursma_2015, Ellsworth_2004, Ethier & Livingston_2004, and Stinziano_2021, with reset frequencies of 68–82% across all crops, higher in soybean (78–92%) than in other crops (7–21%, Table S5). The $R_d = 0$ values should therefore be interpreted only as a fitting safeguard rather than as physiological R_d trait estimates. Enforcing $R_d \geq 0$ caused only minor upward shifts in $V_{cmax,25}$ and J_{25} where $R_d < 0$ occurred (Figs S5, S6), and all results in the main-text use the constrained solutions. Method-specific handling was applied where required. Sharkey_2016 (2.0R) derives J from A_n–Q information; therefore, J_{25} was unavailable for soybean on DOY 167, 215, and 222 (no A_n–Q curves) and this method was excluded only from those dates' statistical tests. Collatz_1991 and Long & Bernacchi_2003 were used only to estimate $V_{cmax,25}$ and were excluded from all J_{25} analyses.

We additionally implemented the optimality-based photosynthetic capacity model of Smith_2019 as an external benchmark. For each site year, the model was driven by daily ERA5-Land forcing (0.1°; temperature, vapor pressure deficit, photosynthetically active radiation) and elevation, and daily $V_{cmax,25}$ and J_{25} were sampled on the A_n–C_i measurement dates for comparison with fitted estimates. This design ensured temporal alignment between the optimality benchmark and the leaf-level observations.

Between-method differences in $V_{cmax,25}$ and J_{25} were tested for each measurement date using Welch's one-way ANOVA. For soybean, $V_{cmax,25}$–J_{25} coordination was evaluated by linear regression (J_{25} = slope × $V_{cmax,25}$ + intercept) and summarized by R^2 and ratio of performance to deviation (RPD), defined as the ratio of SD to RMSE, where SD is the standard deviation of observed J_{25} and RMSE is the regression prediction error; for the nonsoybean datasets (single date per site year), coordination was summarized using the $J_{25}/V_{cmax,25}$ ratio. Simultaneous Chl fluorescence measurements during the A_n–C_i protocol provided an external consistency check via ETR_{max}, defined for each replicate as the maximum fluorescence-derived ETR across CO_2 steps under the imposed saturating PPFD. Fitted J (at the measurement leaf temperature) was compared against ETR_{max} as a reference, noting that ETR_{max} is not a direct estimate of FvCB J.

Sensitivity analysis of $V_{cmax,25}$ and J_{25} estimation

We conducted two complementary sensitivity analyses to attribute cross-configuration variation in $V_{cmax,25}$ and J_{25} to

© 2026 The Author(s).
New Phytologist © 2026 New Phytologist Foundation.

14698137, 0, Downloaded from https://nph.onlinelibrary.wiley.com/doi/10.1111/nph.71358 by Northwest Agri & Forestry, Wiley Online Library on [14/06/2026]. See the Terms and Conditions (https://onlinelibrary.wiley.com/terms-and-conditions) on Wiley Online Library for rules of use; OA articles are governed by the applicable Creative Commons License

differences in fitting assumptions. All crop datasets were included; for soybean, only the 2019 season was used because the 2019 and 2020 measurements followed the same protocol, while 2019 provided denser temporal coverage.

First, we performed a one-at-a-time (OAT) analysis using Sharkey_2007 as the baseline configuration, perturbing a single methodological component per run (Table 2; Eqns 5–8). We examined six process-level assumptions: g_m treatment (∞; gas exchange only; gas exchange + Chl fluorescence), R_d treatment (linear fitting; nonlinear fitting; fixed fraction of V_{cmax}), Γ* formulation (alternative implementations), temperature-response function $k(T)$ (Arrhenius; Q_{10}; peaked Arrhenius), TPU inclusion (on/off), and limiting-rate selection (full-curve; quadratic smoothing; C_i-threshold partitioning). We additionally tested discrete kinetic choices by swapping (1) paired $K_{c,25}$–$K_{o,25}$ sets and (2) Γ^*_{25} values used across methods (Table 2). This design isolates how replacing one assumption relative to Sharkey_2007 shifts fitted $V_{cmax,25}$ and J_{25}.

Second, we quantified relative contributions within a variance-based framework. For process assumptions, we followed the global conditional-expectation approach of Dai *et al.* (2017): the focal process was varied across its alternatives while all other processes were averaged over their available formulations, yielding first-order sensitivity indices (variance of the conditional-expectation normalized by total variance). For kinetic assumptions (treated as discrete factors), we applied ANOVA-based variance decomposition (Miller, 1986; Cottingham *et al.*, 2005) focusing on the paired $K_{c,25}$–$K_{o,25}$ sets and Γ^*_{25}. To avoid overweighting crops with more observations, process sensitivities were computed within each crop and then averaged across crops with equal weights. Higher-order interactions were not evaluated; first-order effects captured the majority of total variance in our analyses (Walker *et al.*, 2021).

SCOPE simulations from leaf-level A_n to seasonal soybean GPP

To quantify how method-specific $V_{cmax,25}$ estimates propagate into forward simulations (rather than to rank fitting methods), we used SCOPE to simulate leaf-level A_n for all crops and seasonal canopy GPP for soybean. SCOPE couples radiative transfer, energy balance, and biochemical modules (Van der Tol *et al.*, 2009; Yang *et al.*, 2021) and has been widely used to simulate ecosystem GPP and its environmental responses (Bayat *et al.*, 2018; Chen *et al.*, 2025; Wu *et al.*, 2025). In SCOPE, $V_{cmax,25}$ is the prescribed biochemical input, whereas electron transport, R_d, and Γ* are computed internally using SCOPE's default formulations; all other biochemical, stomatal, radiative-transfer, and canopy-structure settings were kept at their SCOPE defaults unless stated otherwise. Full biochemical-module details (e.g. the J formulation, R_d parameterization) are provided in Methods S2.

We ran two coefficient scenarios that differ only in Rubisco-kinetic and Γ* conventions ($K_{c,25}$, $K_{o,25}$, and Γ^*_{25}). In the as-implemented scenario, each fitting configuration retained its native $K_{c,25}$–$K_{o,25}$ set and Γ^*_{25} convention, and the resulting $V_{cmax,25}$ estimates were transferred directly into SCOPE. In the parameter-matched scenario, we replaced the fitting-side $K_{c,25}$–$K_{o,25}$ and Γ^*_{25} with SCOPE-consistent values ($K_{c,25} = 40.5$ Pa, $K_{o,25} = 27.9$ kPa, $\Gamma^*_{25} = 4.3$ Pa) and refit the curves to obtain matched $V_{cmax,25}$ before forward simulation. Because the as-implemented scenario reflects common practice, we report it in the main text, while the parameter-matched scenario is provided as a control analysis in the Supporting Information.

Leaf-level A_n simulations were performed by (1) inverting each observed A_n_obs–C_i curve using the SCOPE biochemical module to obtain a self-consistent reference $V_{cmax,25}$, and then rerunning SCOPE forward to generate A_n_Reference; and (2) running SCOPE forward using method-specific $V_{cmax,25}$ to generate A_n simulations. Deviations from observations were quantified as absolute and relative errors over the full A_n–C_i curve and, separately, at $C_a = 400$ μmol mol^{-1}:

$$\Delta A_n = A_{n,i} - A_n\_obs \quad \text{Eqn 9a}$$

$$\Delta A_{n,\%} = \frac{A_{n,i} - A_n\_obs}{A_n\_obs} \times 100\% \quad \text{Eqn 9b}$$

where $A_{n,i}$ is the simulated assimilation using method-i $V_{cmax,25}$ and A_n_obs is the observed assimilation. Simulations used replicate $V_{cmax,25}$ for each method and date, and uncertainty envelopes were generated as the mean ± 1 SD of replicate-based SCOPE simulations for each date. Soybean on 19 July 2019 is shown as an illustrative example, whereas other crops correspond to their measurement days.

Seasonal GPP simulations were conducted only for soybean (2019), which provided continuous meteorological forcing and canopy inputs for driving SCOPE across the growing season. Because A_n–C_i measurements were available only on discrete dates, daily $V_{cmax,25}$ trajectories were constructed for each fitting configuration by piecewise linear interpolation between adjacent measurement dates (holding values constant before the first and after the last measurement). These daily $V_{cmax,25}$ series were then used to drive seasonal SCOPE GPP. A self-consistency reference trajectory (GPP_Reference) was obtained by driving SCOPE with the reference-inverted $V_{cmax,25}$ series under the same forward settings, and method-specific GPP deviations were quantified in absolute and relative terms:

$$\Delta GPP = GPP_i - GPP\_Reference \quad \text{Eqn 10a}$$

$$\Delta GPP_{\%} = \frac{GPP_i - GPP\_Reference}{GPP\_Reference} \times 100\% \quad \text{Eqn 10b}$$

where GPP_i denotes simulations using method-i $V_{cmax,25}$ and GPP_Reference denotes the corresponding self-consistency reference simulation. Seasonal uncertainty envelopes were generated by propagating the mean ± 1 SD range of $V_{cmax,25}$ through the interpolation and forward simulation steps.

© 2026 The Author(s).
New Phytologist © 2026 New Phytologist Foundation.

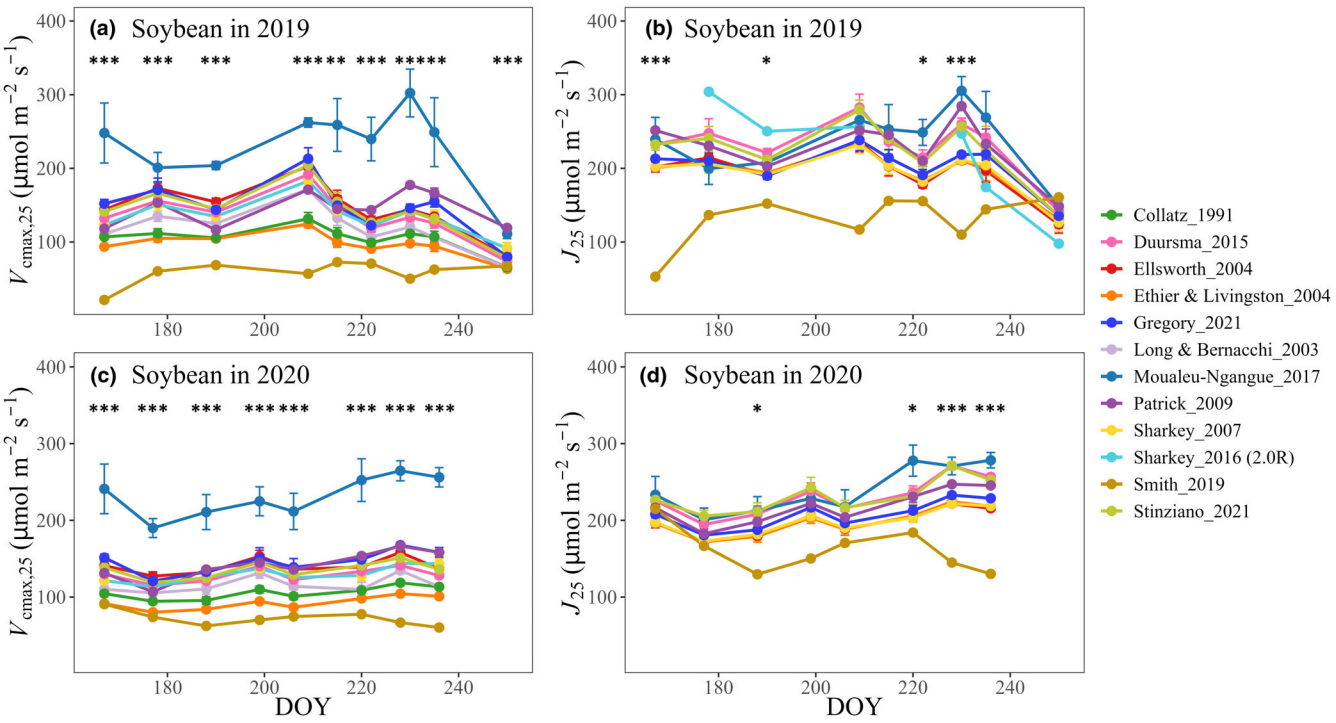

Fig. 1 Seasonal dynamics of soybean photosynthetic capacity at 25°C in 2019 and 2020 derived from multiple A_n–C_i fitting configurations. (a) $V_{cmax,25}$ and (b) J_{25} across nine dates (day of year, DOY) in 2019. (c) $V_{cmax,25}$ and (d) J_{25} across eight dates in 2020. Points represent method-specific means across replicate leaves measured on the same date, and error bars denote SE across replicates. Asterisks indicate significant among-method differences at each date based on Welch's one-way ANOVA (*, $P < 0.05$; **, $P < 0.01$; ***, $P < 0.001$). Sharkey_2007 and Sharkey_2016 (2.0R) use the same procedure to estimate $V_{cmax,25}$ from A_n–C_i curves and therefore give identical $V_{cmax,25}$ values. Sharkey_2016 (2.0R) derives J_{25} from light-response information and thus has no J_{25} estimates on DOY 167, 215, and 222 in 2019 because A_n–Q curves were unavailable. Long & Bernacchi_2003 and Collatz_1991 do not provide J_{25} and are therefore omitted from panels (b) and (d).

Results

Cross-method variation in estimated $V_{cmax,25}$, J_{25}, and their relationship

For soybean, both $V_{cmax,25}$ and J_{25} varied seasonally in 2019 and 2020, but their magnitudes differed strongly among methods (Fig. 1). In 2019, $V_{cmax,25}$ spanned *c.* 20–302 μmol m^{-2} s^{-1} across dates and methods. Smith_2019 and Moualeu-Ngangue_2017 produced the lowest and highest values, respectively. On DOY 230, most other methods fell between 98 and 177 μmol m^{-2} s^{-1}. In 2020, a similar pattern emerged. Across both years, $V_{cmax,25}$ differed significantly among methods on all observation dates, with most dates reaching $P < 0.001$ (Fig. 1a,c).

Soybean J_{25} also differed among methods, but over a narrower range than $V_{cmax,25}$. In 2019, J_{25} ranged from 53 to 305 μmol m^{-2} s^{-1}, with Smith_2019 generally yielding the lowest values, whereas Duursma_2015, Patrick_2009, Moualeu-Ngangue_2017, and Sharkey_2016 (2.0R) occupied the upper range. On DOY 230, J_{25} varied from *c.* 110 to 305 μmol m^{-2} s^{-1}. In 2020, a pattern similar to that in 2019 emerged. Among-method differences were significant on four of nine dates in 2019 and four of eight dates in 2020 (Fig. 1b,d). V_{cmax} and J at measurement temperature showed patterns similar to those at 25°C (Fig. S7).

Across the other crops, method-dependent differences were also substantial (Fig. 2). $V_{cmax,25}$ ranged from 82 to 262, 71 to 205, 68 to 290, and 79 to 359 μmol m^{-2} s^{-1} in perennial ryegrass, red clover, winter wheat (Yucheng), and winter wheat (Yangling), respectively. For J_{25}, the corresponding ranges were 104–297, 135–332, 109–412, and 122–343 μmol m^{-2} s^{-1}, respectively. The distribution of higher estimates varied among crops: Moualeu-Ngangue_2017 and Patrick_2009 tended to produce higher values in perennial ryegrass and winter wheat (Yangling), whereas Patrick_2009, Duursma_2015, and Sharkey_2016 (2.0R) were among the higher estimates in red clover and winter wheat (Yucheng). Method effects were significant for both parameters across all crops, with especially strong effects on $V_{cmax,25}$ (all $P < 0.001$). V_{cmax} and J at measurement temperature showed patterns similar to those at 25°C (Fig. S8).

Comparison with ETR_{max} provided an external physiological reference for fitted J estimates (Fig. S9; Table S6). Across soybean and the other crops, regression slopes between J and ETR_{max} ranged from 0.81 to 1.26 and 0.47 to 2.00, respectively. When all crops were pooled, slopes ranged 0.87–1.29. In soybean, ETR_{max} generally lay near the upper range of fitted J, whereas in the other crops, it fell within the distribution rather than at the extremes.

In soybean, the fitted $V_{cmax,25}$–J_{25} relationship differed markedly among methods, with slopes ranging from 0.75 (Gregory_2021) to 2.80 (Smith_2019) and intercepts from −52 to

© 2026 The Author(s).
New Phytologist © 2026 New Phytologist Foundation.

14698137, 0, Downloaded from https://nph.onlinelibrary.wiley.com/doi/10.1111/nph.71358 by Northwest Agri & Forestry, Wiley Online Library on [14/06/2026]. See the Terms and Conditions (https://onlinelibrary.wiley.com/terms-and-conditions) on Wiley Online Library for rules of use; OA articles are governed by the applicable Creative Commons License

14698137, 0, Downloaded from https://nph.onlinelibrary.wiley.com/doi/10.1111/nph.71358 by Northwest Agri & Forestry, Wiley Online Library on [14/06/2026]. See the Terms and Conditions (https://onlinelibrary.wiley.com/terms-and-conditions) on Wiley Online Library for rules of use; OA articles are governed by the applicable Creative Commons License

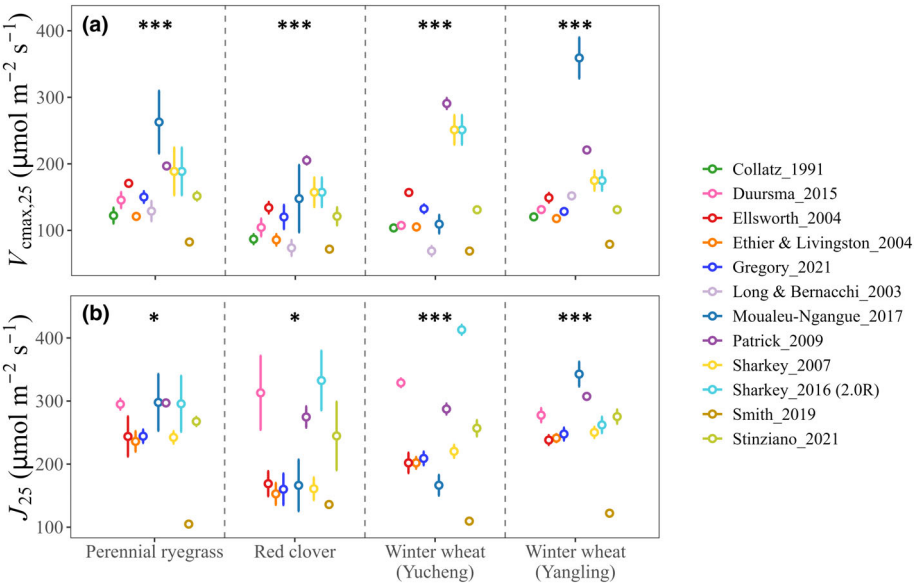

Fig. 2 Cross-species comparison of fitted photosynthetic capacity at 25°C using different A_n–C_i fitting configurations. (a) $V_{cmax,25}$ and (b) J_{25} for perennial ryegrass, red clover, winter wheat (Yucheng), and winter wheat (Yangling). Points represent method-specific means across replicate leaves, and error bars denote SE across replicates. Asterisks indicate significant among-method effects within each crop based on Welch's one-way ANOVA (*, $P < 0.05$; **, $P < 0.01$; ***, $P < 0.001$).

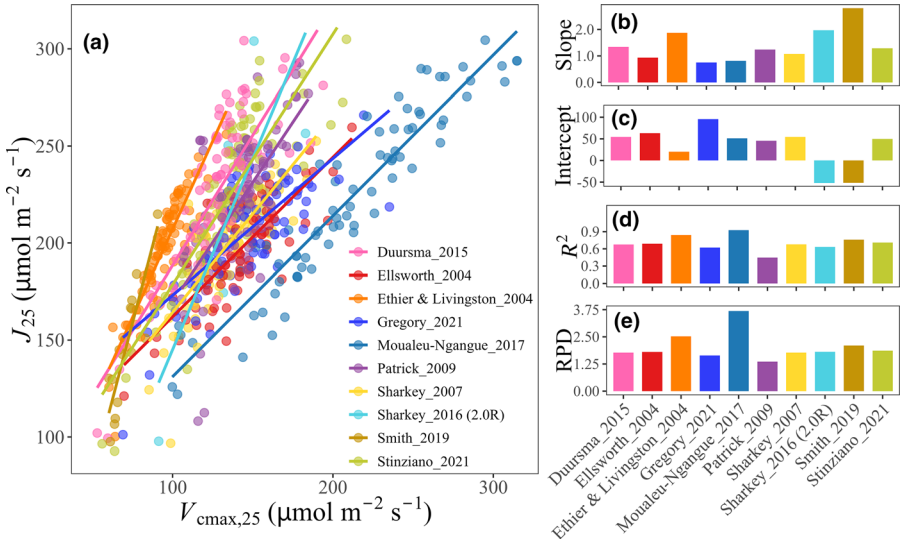

Fig. 3 Relationship between $V_{cmax,25}$ and J_{25} for soybean in 2019 and 2020 across dates, by fitting configuration. (a) Scatter plots and ordinary least-squares regression lines for each method (J_{25} = slope × $V_{cmax,25}$ + intercept). (b) Method-specific slopes, (c) intercepts, (d) coefficient of determination (R^2), and (e) ratio of performance to deviation (RPD), used here as goodness-of-fit metrics for the coordination relationship.

95 (Fig. 3). R^2 and RPD ranged from 0.45 to 0.93 and 1.36 to 3.69, respectively, with the highest values for Moualeu-Ngangue_2017 and the lowest for Patrick_2009. For the other crops, coordination between J_{25} and $V_{cmax,25}$ was summarized using the ratio $J_{25}/V_{cmax,25}$ (Fig. 4). This ratio ranged from 1.15 to 2.04 in perennial ryegrass, 1.05 to 2.97 in red clover, 0.89 to 3.07 in winter wheat (Yucheng), and 0.97 to 2.12 in winter wheat (Yangling). Duursma_2015 was among the highest-ratio methods across crops (>2.0), whereas Sharkey_2007, Patrick_2009, and Moualeu-Ngangue_2017 generally occupied the lower range.

Sensitivity of processes and parameters driving cross-method variation in $V_{cmax,25}$ and J_{25}

Sensitivity analyses showed that cross-method variation in fitted $V_{cmax,25}$ and J_{25} was primarily driven by g_m treatment and limiting-rate selection among the process assumptions, while the paired $K_{c,25}$–$K_{o,25}$ sets also contributed substantially, especially to $V_{cmax,25}$ (Figs 5–7). By contrast, R_d, Γ*, $k(T)$, TPU, and Γ^*_{25} had comparatively minor effects.

In the OAT for soybean in 2019, g_m produced the largest shifts in both $V_{cmax,25}$ and J_{25} (Fig. 5d,j). Relative to the infinite-g_m assumption, Eqn 5(b) increased $V_{cmax,25}$ and J_{25} by 46–109 and 30–80 μmol m^{-2} s^{-1}, respectively, whereas Eqn 5(a) remained close to the infinite g_m case (< 20 μmol m^{-2} s^{-1}). The corresponding soybean process estimates (Fig. S10) showed R_d, g_m, and Γ* under different assumptions. Eqn 5(b) generally produced lower g_m than Eqn 5(a), consistent with its higher $V_{cmax,25}$ and J_{25}.

Limiting-rate selection was the second largest process source of variation (Fig. 5f,l). For $V_{cmax,25}$, the quadratic formulation consistently yielded the lowest values, 39–72 μmol m^{-2} s^{-1} lower than the C_i-threshold and full-curve schemes. For J_{25}, the effect

© 2026 The Author(s).
New Phytologist © 2026 New Phytologist Foundation.

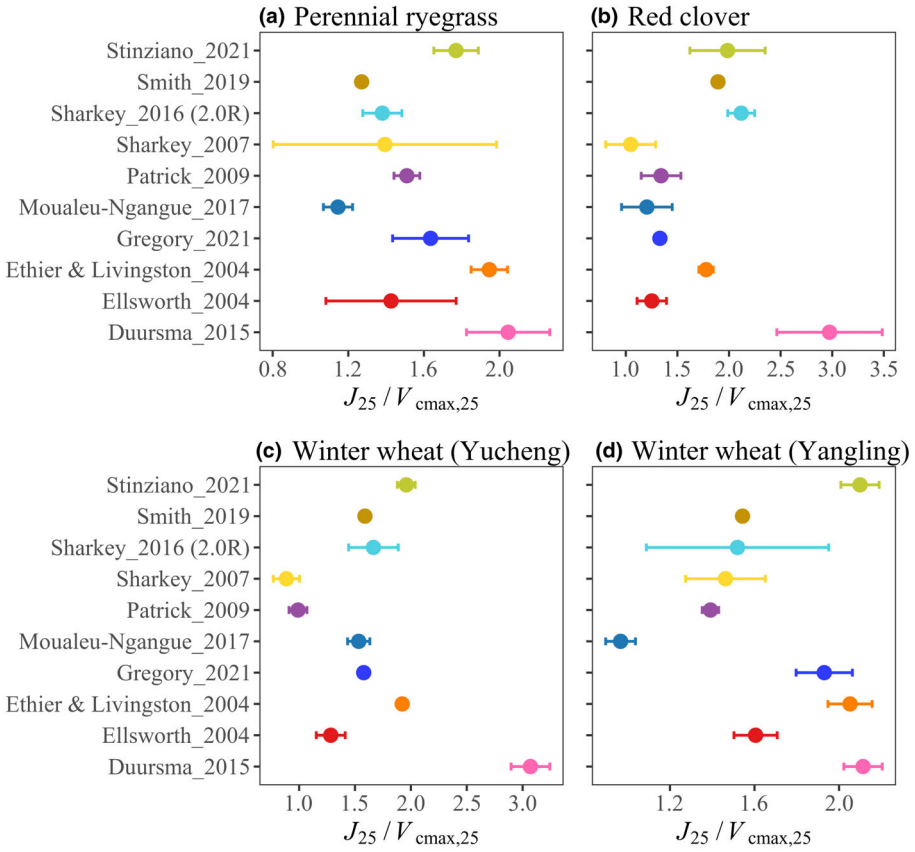

Fig. 4 Method-specific ratios of J_{25} to $V_{cmax,25}$ for (a) perennial ryegrass, (b) red clover, (c) winter wheat (Yucheng), and (d) winter wheat (Yangling). Points indicate method-specific mean $J_{25}/V_{cmax,25}$ ratios across replicate leaves, and error bars denote SE across replicates. Because the Smith_2019 method yielded only one value per day, no error bars are shown for this method; all other methods include error bars.

was smaller but still evident, with the quadratic formulation lower by 9–48 μmol m^{-2} s^{-1}. The threshold-based and full-curve schemes yielded similar results, mostly differing by < 20 μmol m^{-2} s^{-1}.

Among the remaining process assumptions, R_d formulation had a moderate effect on $V_{cmax,25}$ but only a small effect on J_{25} (Fig. 5b,h). Eqn 6(a) produced the highest $V_{cmax,25}$ and J_{25}, whereas the other estimates clustered closely. Different Γ* formulations caused smaller but measurable shifts (Fig. 5a,g), ranging from 6 to 35 and 4 to 17 μmol m^{-2} s^{-1} for $V_{cmax,25}$ and J_{25}, respectively. The effect of $k(T)$ was similarly modest (Fig. 5e,k), with differences of 5–11 and 4–9 μmol m^{-2} s^{-1} for $V_{cmax,25}$ and J_{25}, respectively. TPU had the smallest effect (Fig. 5c,i), within 1–15 μmol m^{-2} s^{-1} for both parameters.

Cross-crop analyses showed broadly similar patterns, although the magnitude of the g_m effect differed among species (Fig. S11; corresponding R_d, g_m, and Γ* estimates are shown in Fig. S12). In winter wheat (Yangling), Eqn 5(b) produced the highest $V_{cmax,25}$ and J_{25}. In perennial ryegrass and red clover, the difference between Eqns 5(a) and Eqns 5(b) was smaller, and both exceeded the infinite-g_m assumption. In winter wheat (Yucheng), Eqn 5(a) exceeded Eqn 5(b) for both $V_{cmax,25}$ and J_{25}. Limiting-rate selection showed the same general ordering across crops as in soybean. R_d, Γ*, $k(T)$, and TPU had minor effects across non-soybean datasets.

Parameter perturbations showed that discrete kinetic parameters also affected $V_{cmax,25}$ and J_{25} (Figs 6, S13). In soybean, replacing the paired $K_{c,25}$–$K_{o,25}$ parameter sets changed $V_{cmax,25}$ by 36–73 μmol m^{-2} s^{-1}, whereas changing Γ^*_{25} caused only small shifts (< 25 μmol m^{-2} s^{-1} for both $V_{cmax,25}$ and J_{25}). Other crops showed a similar pattern (Fig. S13).

Variance-based sensitivity analysis confirmed these patterns (Fig. 7). Across crop ensembles, g_m showed the highest first-order sensitivity for both $V_{cmax,25}$ and J_{25} (*c.* 0.64 and 0.61), followed by limiting-rate selection (*c.* 0.21 and 0.19). The remaining processes had relatively small effects, with sensitivity indices of Γ*, k (T), R_d, and TPU all below *c.* 0.12 for $V_{cmax,25}$ and 0.18 for J_{25}. At the parameter level, the paired $K_{c,25}$–$K_{o,25}$ sets explained 0.33 of the variance in $V_{cmax,25}$, whereas Γ^*_{25} explained 0.04. Thus, both analyses identified g_m and limiting-rate selection as the dominant process sources of cross-method divergence, and the paired $K_{c,25}$–$K_{o,25}$ sets as the dominant kinetic-choice source.

Effects of $V_{cmax,25}$ parameterization on A_n and GPP simulations

Under the as-implemented scenario, the SCOPE-based self-consistency reference (A_n_Reference) closely reproduced the observed A_n–C_i curves across all four crops (Fig. 8), with deviations from A_n_obs generally within 0–2.4 μmol m^{-2} s^{-1} over the full C_i range. Simulations driven by method-specific $V_{cmax,25}$ showed clear crop- and method-dependent offsets. Typically, Moualeu-Ngangue_2017 produced the highest curves, whereas Long & Bernacchi_2003, Collatz_1991, and Ethier &

© 2026 The Author(s).
New Phytologist © 2026 New Phytologist Foundation.

14698137, 0, Downloaded from https://nph.onlinelibrary.wiley.com/doi/10.1111/nph.71358 by Northwest Agri & Forestry, Wiley Online Library on [14/06/2026]. See the Terms and Conditions (https://onlinelibrary.wiley.com/terms-and-conditions) on Wiley Online Library for rules of use; OA articles are governed by the applicable Creative Commons License

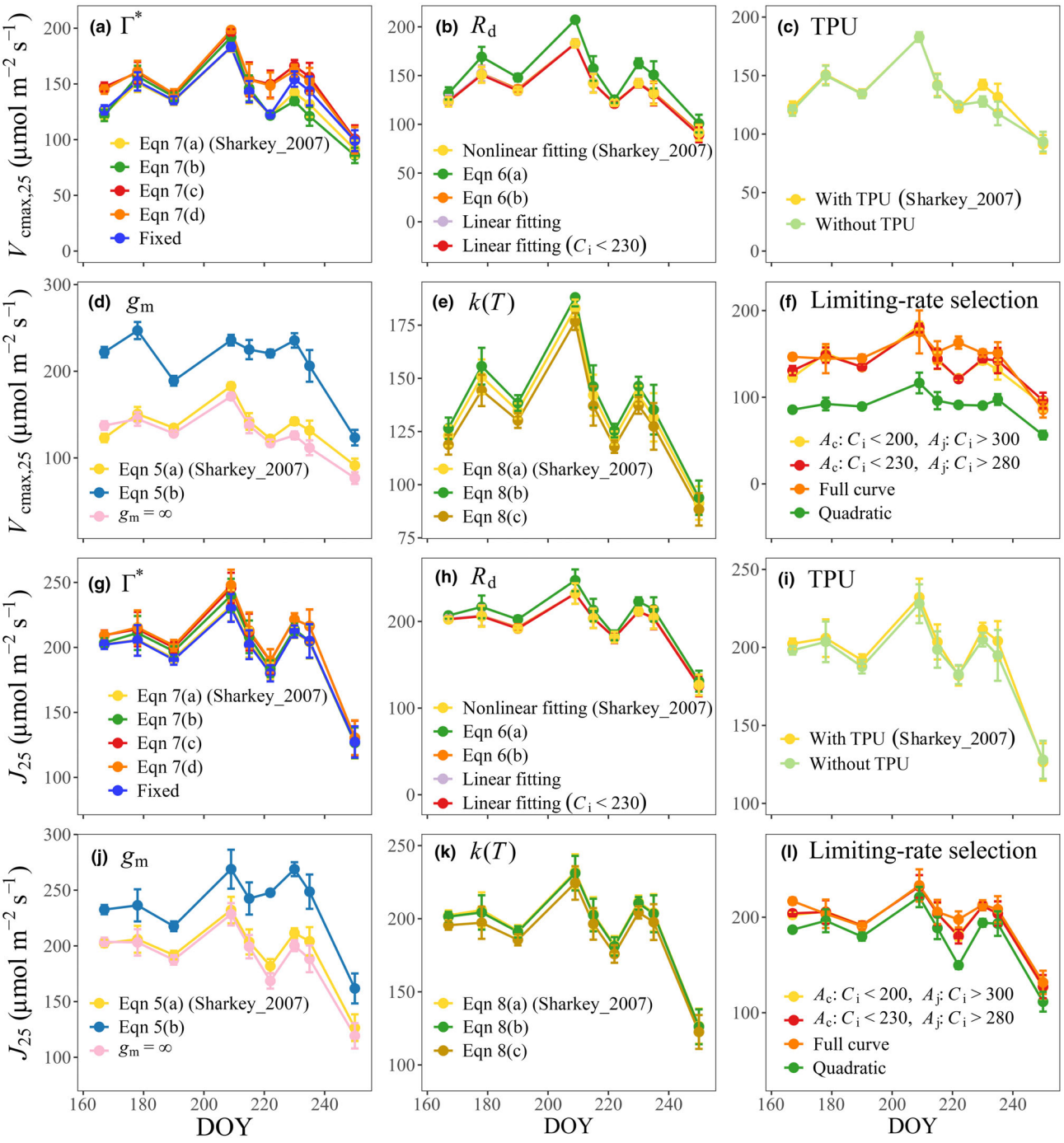

Fig. 5 One-at-a-time sensitivity analysis of six process assumptions on fitted $V_{cmax,25}$ and J_{25} during the 2019 soybean growing season. Panels (a–f) show the effects on $V_{cmax,25}$ and panels (g–l) show the corresponding effects on J_{25}. The six perturbed process assumptions are Γ* formulation, R_d treatment, triose phosphate utilization (TPU) inclusion, g_m treatment, temperature-response function $k(T)$, and limiting-rate selection. Points represent means across replicate leaves and error bars denote SE. DOY, day of year.

Livingston_2004 produced the lowest. Under the parameter-matched scenario (Fig. S14), the overall crop-specific ranking remained similar, although the spread narrowed in some cases.

These offsets were quantified in Fig. 9 using the mean deviation over the full A_n–C_i curve. Under the as-implemented scenario, the bias of A_n_Reference was 0–9%. The relative bias percentages of A_n in soybean, perennial ryegrass, red clover, winter wheat (Yucheng), and winter wheat (Yangling) ranged from −30% to +26%, −31% to +25%, −55% to −6%, −68% to +7%, and − 17% to +81%, respectively. The parameter-matched control (Fig. S15) preserved the same crop-specific error ranking but reduced the error range in some cases. The relative

© 2026 The Author(s).
New Phytologist © 2026 New Phytologist Foundation.

14698137, 0, Downloaded from https://nph.onlinelibrary.wiley.com/doi/10.1111/nph.71358 by Northwest Agri & Forestry, Wiley Online Library on [14/06/2026]. See the Terms and Conditions (https://onlinelibrary.wiley.com/terms-and-conditions) on Wiley Online Library for rules of use; OA articles are governed by the applicable Creative Commons License

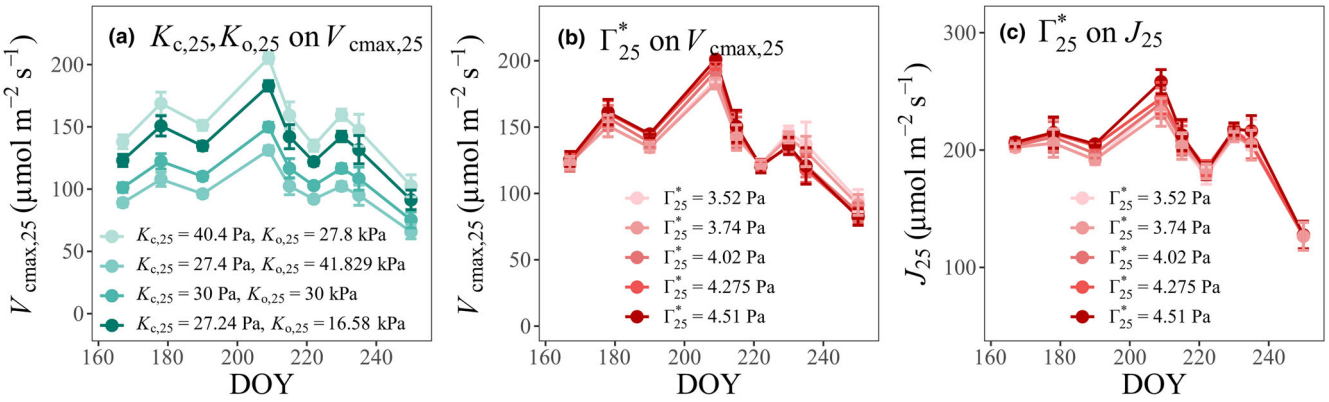

Fig. 6 One-at-a-time sensitivity analysis of discrete kinetic choices on fitted $V_{cmax,25}$ and J_{25} during the 2019 soybean growing season. (a) Effects of alternative paired $K_{c,25}$–$K_{o,25}$ sets on $V_{cmax,25}$; (b) effects of alternative Γ^*_{25} values on $V_{cmax,25}$; (c) effects of alternative Γ^*_{25} values on J_{25}. Points represent means across replicate leaves and error bars denote SE. DOY, day of year.

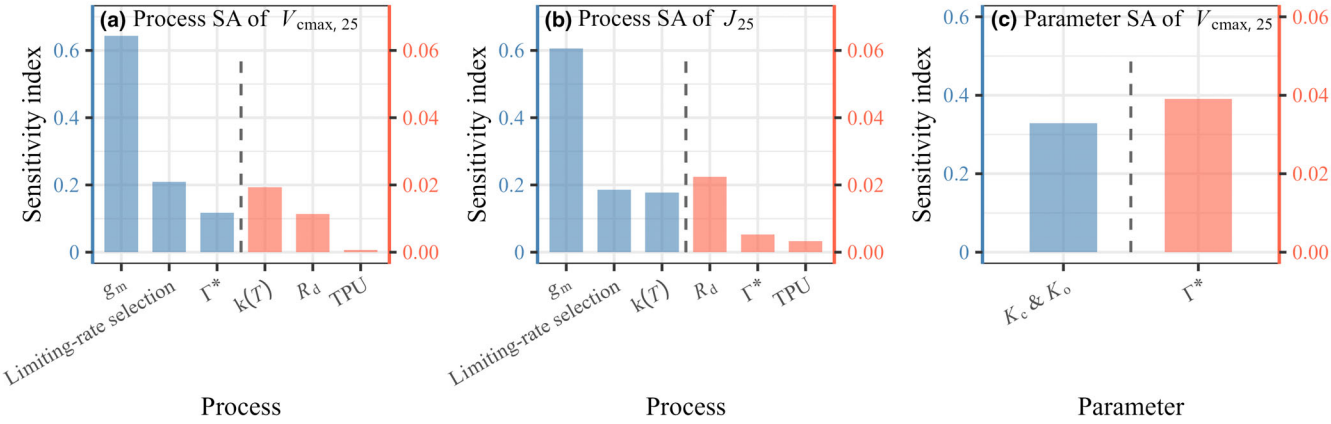

Fig. 7 Variance-based sensitivity analysis (SA) of fitted $V_{cmax,25}$ and J_{25} across crop ensembles. (a) First-order process sensitivity indices for $V_{cmax,25}$; (b) first-order process sensitivity indices for J_{25}; (c) ANOVA-based variance decomposition for discrete kinetic choices, including paired $K_{c,25}$–$K_{o,25}$ sets and Γ^*_{25}. Blue and red bars correspond to the left and right *y*-axes, respectively; dashed vertical lines separate groups plotted against different *y*-axes scales.

bias percentage ranged from *c.* −23% to +46% in winter wheat (Yangling). The largest positive bias decreased most clearly in winter wheat (Yangling; *c.* 30%). Results at $C_a = 400$ μmol mol^{-1} were consistent with the full A_n–C_i curve analysis (Fig. S16: as-implemented; Fig. S17: parameter-matched). Overall, parameter matching reduced some deviations, particularly in winter wheat (Yangling), but did not alter the overall method ranking.

Seasonal soybean GPP simulations under the as-implemented scenario showed a similar but more muted propagation of $V_{cmax,25}$ differences to the canopy scale (Fig. 10). During the growing season, GPP_Reference increased initially and then declined. Across methods, simulated daily GPP generally remained close to this reference trajectory, but systematic offsets were still evident. Moualeu-Ngangue_2017 and Patrick_2009 both showed relatively large positive biases (+10% to +20%). By contrast, Smith_2019 showed the largest negative deviations, with values reaching *c.* −34% during mid-season. Collatz_1991, Ethier & Livingston_2004, and Long & Bernacchi_2003 also underestimated GPP, but with smaller magnitudes (within −12%). Other methods mostly remained within ±5% of the reference (Fig. 10d). The parameter-matched control showed the same overall seasonal ordering of GPP trajectories (Fig. S18). Overall, method-dependent differences in fitted $V_{cmax,25}$ propagated into leaf-level A_n and seasonal GPP, with greater relative spread in A_n. Harmonizing $K_{c,25}$, $K_{o,25}$, and Γ^*_{25} reduced, but did not eliminate, this spread.

Discussion

Our results show that A_n–C_i fitting method choice is a major source of variability in fitted $V_{cmax,25}$, J_{25}, their inferred coordination, and downstream photosynthesis simulations. Across crops, methods differed widely in parameter magnitude and transferability, largely driven by differences in process treatments and kinetic assumptions. These findings indicate that photosynthetic capacity estimates are strongly conditioned by the fitting framework. In the following sections, we discuss the main drivers of cross-method variation, the implications for forward simulations

© 2026 The Author(s).
New Phytologist © 2026 New Phytologist Foundation.

14698137, 0, Downloaded from https://nph.onlinelibrary.wiley.com/doi/10.1111/nph.71358 by Northwest Agri & Forestry, Wiley Online Library on [14/06/2026]. See the Terms and Conditions (https://onlinelibrary.wiley.com/terms-and-conditions) on Wiley Online Library for rules of use; OA articles are governed by the applicable Creative Commons License

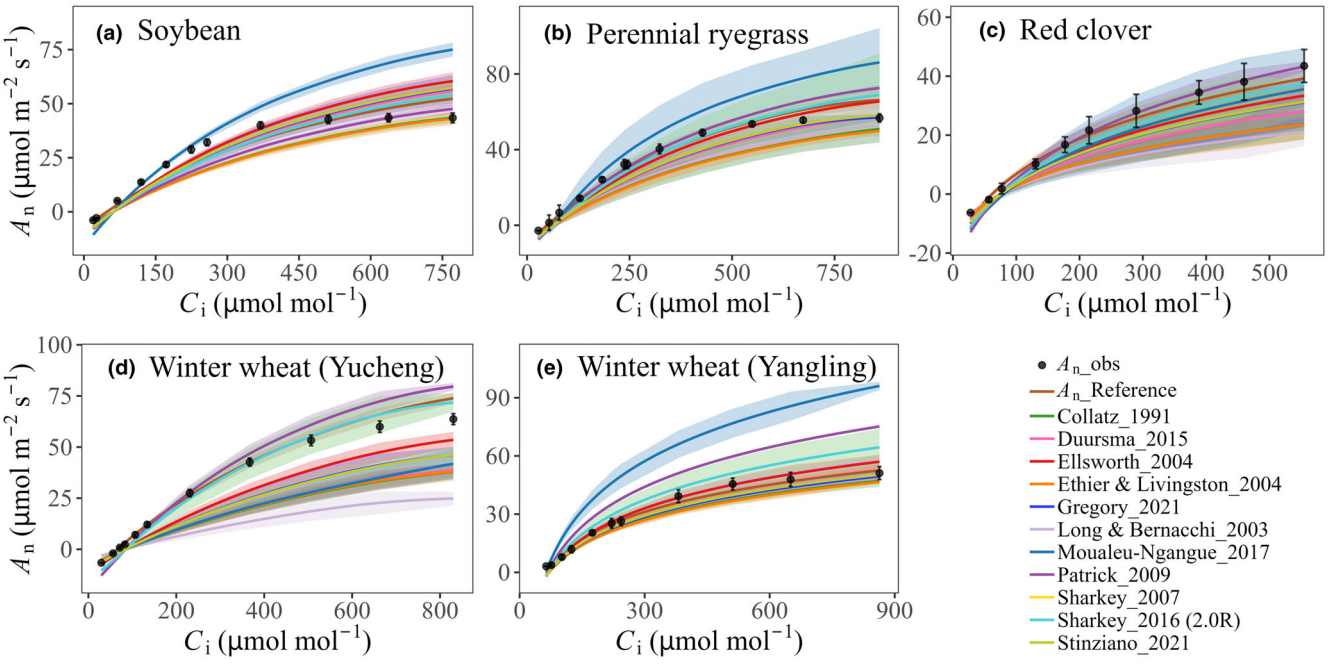

Fig. 8 Observed and simulated A_n–C_i response curves under the as-implemented scenario, in which each fitting tool retained its native $K_{c,25}$, $K_{o,25}$, and Γ^*_{25} settings before $V_{cmax,25}$ was transferred directly into Soil-Canopy Observation, Photochemistry and Energy (SCOPE). (a) Soybean; (b) perennial ryegrass; (c) red clover; (d) winter wheat (Yucheng); (e) winter wheat (Yangling). Black points represent observed assimilation rates (A_n_obs). The brown line (A_n_Reference) denotes the self-consistency reference obtained by inverting $V_{cmax,25}$ from the observed A_n–C_i curves using the SCOPE biochemical module and then rerunning SCOPE in forward mode. Colored lines show simulated A_n–C_i curves using method-specific $V_{cmax,25}$ estimates. For soybean, 19 July 2019 is shown as the illustrative example. Shaded bands indicate the uncertainty range derived from mean ± 1 SD of calculated outputs based on $V_{cmax,25}$ from replicate leaves measured on the same date.

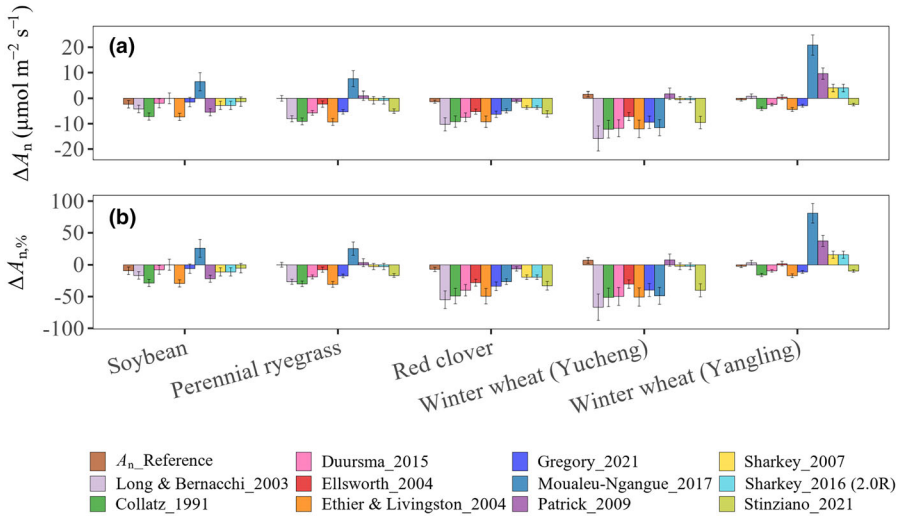

Fig. 9 Deviations between simulated assimilation rates and observed assimilation rates under the as-implemented scenario across the full A_n–C_i response curve. (a) Absolute deviations (ΔA_n, μmol m^{-2} s^{-1}) and (b) relative deviations ($\Delta A_{n,\%}$). Errors were calculated from replicate means, and error bars denote propagated uncertainty from replicate SD of $V_{cmax,25}$.

and parameter transferability, the practical interpretation of method differences, and the limitations and outlook of this study.

Drivers of cross-method variation in fitted $V_{cmax,25}$ and J_{25}

The cross-method spread in fitted $V_{cmax,25}$ and J_{25} reflects systematic differences in process treatments and kinetic assumptions. Although the exact rankings differed, both the OAT and the variance-based sensitivity analysis identified g_m, limiting-rate selection, and the adopted kinetic parameterization as the primary sources of variation (Farquhar *et al.*, 1980; von Caemmerer, 2000; Walker *et al.*, 2021), whereas $k(T)$, Γ*, R_d, and TPU acted mainly as secondary modifiers (Figs 5–7, S11–S13).

Among the process assumptions, g_m exerted the strongest influence on both $V_{cmax,25}$ and J_{25}, although the magnitude of its

© 2026 The Author(s).
New Phytologist © 2026 New Phytologist Foundation.

14698137, 0, Downloaded from https://nph.onlinelibrary.wiley.com/doi/10.1111/nph.71358 by Northwest Agri & Forestry, Wiley Online Library on [14/06/2026]. See the Terms and Conditions (https://onlinelibrary.wiley.com/terms-and-conditions) on Wiley Online Library for rules of use; OA articles are governed by the applicable Creative Commons License

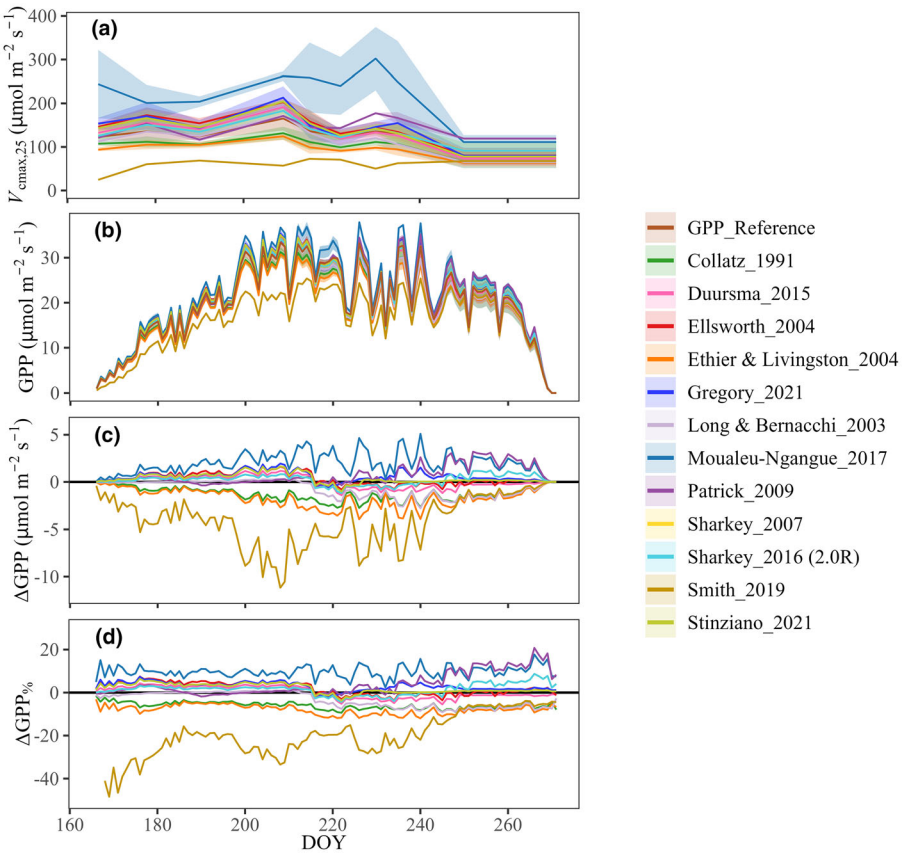

Fig. 10 Effects of method-specific $V_{cmax,25}$ trajectories on soybean gross primary productivity (GPP) simulated with Soil-Canopy Observation, Photochemistry and Energy (SCOPE) under the as-implemented scenario in 2019. (a) Daily $V_{cmax,25}$ trajectories used to drive SCOPE. (b) Daily GPP simulated by SCOPE under each $V_{cmax,25}$ input. (c) Absolute deviations from the self-consistency reference trajectory (ΔGPP, µmol m^{-2} s^{-1}). (d) Relative deviations from the reference trajectory (ΔGPP$_{\%}$). The brown line denotes GPP_Reference. Shaded bands in panels (a) and (b) indicate uncertainty ranges propagated from mean ± 1 SD of $V_{cmax,25}$ across replicate leaves. Meteorological forcing and canopy-structural inputs followed Wu *et al*. (2022).

effect differed among crops and was often slightly larger for $V_{cmax,25}$ than for J_{25}. This is mechanistically expected because finite g_m changes the relationship between C_i and C_c, and thus the effective substrate concentration for inferring carboxylation- and electron-transport-related capacities (Ethier & Livingston, 2004; Niinemets *et al.*, 2009; Yin & Struik, 2009). In practice, methods that estimate g_m explicitly can shift part of the observed curvature of the A_n–C_i response between biochemical limitation and internal CO_2 diffusion. In our dataset, this was most evident under fluorescence-aided g_m. Moualeu-Ngangue_2017, which combines gas exchange and Chl fluorescence to estimate g_m, frequently produced the smallest g_m and among the largest fitted $V_{cmax,25}$ and J_{25}.

Limiting-rate selection was the second major process-level driver. Methods partition the same A_n–C_i observations differently (Walker *et al.*, 2021). In our analyses, this affected $V_{cmax,25}$ more strongly than J_{25}, likely because smoothing or threshold rules mainly alter the low- to intermediate-C_i transition zone, where V_{cmax} is more sensitive to local slope and regime assignment. In our data, quadratic smoothing consistently yielded lower $V_{cmax,25}$ and J_{25} than the threshold-based or full-curve alternatives, consistent with smoothing reducing the capacity required to reproduce the transition region (Collatz *et al.*, 1991; van Diepen *et al.*, 2022).

The remaining factors had smaller but still interpretable effects. The effect of $k(T)$ was slightly larger for J_{25} than for $V_{cmax,25}$, as J_{25} depends directly on temperature normalization, whereas $V_{cmax,25}$ is additionally constrained by low-C_i slope and carboxylation kinetics (Kattge & Knorr, 2007; Kumarathunge *et al.*, 2019). Γ* also shifted both capacities, with a stronger effect on $V_{cmax,25}$ because it directly alters the carboxylation-limited CO_2 response, especially at low-C_i (Bernacchi *et al.*, 2001; Cano *et al.*, 2014). R_d showed a modest influence; constraining negative values to zero and refitting markedly reduced its contribution to cross-method spread. TPU had the weakest effect, consistent with syntheses suggesting that TPU limitation is not a dominant control in typical leaf-level A_n–C_i datasets under current atmospheric CO_2 conditions (Kumarathunge *et al.*, 2019; Rogers *et al.*, 2021).

At the parameter level, the adopted kinetic set, especially the paired $K_{c,25}$–$K_{o,25}$ choice, emerged as another major source of divergence. This factor primarily affects $V_{cmax,25}$ rather than J_{25} because K_c and K_o directly enter the Michaelis–Menten term that defines the V_c-limited branch, whereas J is influenced only indirectly through the shifting balance between Rubisco- and electron-transport-limited assimilation (Brooks & Farquhar, 1985; von Caemmerer, 2000; Bernacchi *et al.*, 2001). Consequently, part of the apparent biological variation in fitted $V_{cmax,25}$ across studies may instead reflect differences in adopted kinetic constants and associated parameter conventions (Long & Bernacchi, 2003; Sharkey *et al.*, 2007).

Importantly, these assumptions affected the two fitted capacities asymmetrically, although the degree of asymmetry was crop dependent. Overall, the between-method spread tended to be

© 2026 The Author(s).
New Phytologist © 2026 New Phytologist Foundation.

14698137, 0, Downloaded from https://nph.onlinelibrary.wiley.com/doi/10.1111/nph.71358 by Northwest Agri & Forestry, Wiley Online Library on [14/06/2026]. See the Terms and Conditions (https://onlinelibrary.wiley.com/terms-and-conditions) on Wiley Online Library for rules of use; OA articles are governed by the applicable Creative Commons License

14698137, 0, Downloaded from https://nph.onlinelibrary.wiley.com/doi/10.1111/nph.71358 by Northwest Agri & Forestry, Wiley Online Library on [14/06/2026]. See the Terms and Conditions (https://onlinelibrary.wiley.com/terms-and-conditions) on Wiley Online Library for rules of use; OA articles are governed by the applicable Creative Commons License

larger for $V_{cmax,25}$ than for J_{25}. Previous studies also show that J estimates are relatively robust to methodological choices, whereas V_{cmax} estimates are more sensitive to assumptions regarding diffusion limitations and kinetic parameterization (Duursma, 2015; Kumarathunge *et al.*, 2019). Method choice therefore also altered the inferred coordination between $V_{cmax,25}$ and J_{25}, indicating that these fitted capacities – and their ratio – remain conditioned by the fitting framework from which they were derived.

Consequences for photosynthesis simulation and parameter transferability

The differences among fitting methods matter not only because they change $V_{cmax,25}$ and J_{25}, but because they affect how readily those parameters can be transferred into forward simulations. Our forward experiments showed that method-dependent spread propagated into simulated leaf-level assimilation and seasonal GPP. Thus the main implication is not simply that fitted capacities differ, but that their downstream usability depends on whether the assumptions used during inversion are compatible with those in the target forward model.

At the leaf scale, the as-implemented and parameter-matched comparisons showed that transferability was only partly controlled by kinetic-coefficient mismatch. The spread in simulated A_n decreased under the parameter-matched setup, but substantial differences remained because method-specific g_m treatment and limiting-rate selection still propagated into different forward responses. Notably, in some cases parameter harmonization slightly increased the spread (Moualeu-Ngangue_2017; Fig. S18). This likely reflects compensatory effects between parameter- and process-level differences: when these act in opposite directions, harmonization disrupts the compensation and amplifies discrepancies. At $C_a = 400\ \mu mol\ mol^{-1}$, method ordering remained broadly consistent with the full A_n–C_i curve (Figs S16, S17), indicating that discrepancies were not confined to the high-C_i region but reflected systematic differences in how fitted capacities represented the overall response. This is particularly relevant for modeling applications because $V_{cmax,25}$ is often treated as a portable summary quantity. Our results instead suggest that this portability is conditional and remains interpretable only within the specific FvCB framework and process assumptions used to derive it.

At the canopy scale, the same inconsistency propagated into GPP, although with smaller relative effects than at the leaf scale (A_n). However, this attenuation from leaf to canopy scale does not imply that method choice becomes unimportant at larger scales; rather, it reflects buffering by canopy radiative transfer, vertical light gradients, and co-limitation across sunlit and shaded leaves, which reduce the direct leverage of leaf-level $V_{cmax,25}$ differences on canopy-integrated carbon gain (van der Tol *et al.*, 2009; Yang *et al.*, 2021). Meanwhile, method-specific offsets remained visible in seasonal GPP, indicating that canopy integration attenuated but did not eliminate fitting-induced differences, while largely preserving their direction and relative ordering. This matters because even modest differences in photosynthetic capacity parameterization can influence modeled GPP and, more broadly, the sensitivity of terrestrial carbon-cycle simulations to climate and trait assumptions (Walker *et al.*, 2017; Rogers *et al.*, 2017a).

From a modeling perspective, the most defensible approach is to estimate $V_{cmax,25}$ and J_{25} under assumptions that are as consistent as possible with the intended forward model. This recommendation is supported by the SCOPE-based reference simulation: A_n_Reference matched A_n_obs within $< 9\%$ across the full C_i range (Fig. 9). When such consistency is feasible, part of the transfer error can be reduced. When it is not, literature-derived values should not be treated as assumption-free truths, but as conditional estimates whose uncertainty includes both fitting uncertainty and structural mismatch between inverse and forward frameworks. In practice, these parameters are better propagated as priors or ensembles of internally consistent configurations rather than as deterministic values.

Method comparison and practical implications

Our results do not support a single universal ranking of fitting methods, because the three evaluation lines used here probe different aspects of method behavior rather than a single ground truth. In the main analyses, the ETR_{max} comparison serves as an independent physiological consistency check for fitted J, whereas the SCOPE forward tests assess the transferability of fitted capacities to a canopy-scale framework. We also introduced a synthetic benchmark, in which A_n–C_i curves were generated from prescribed truth sets under controlled g_m and TPU configurations and then refit by the different methods (Methods S3). These lines of evidence are therefore complementary rather than interchangeable.

The ETR_{max} comparison is useful mainly for identifying relatively conservative or aggressive J estimates. Moualeu-Ngangue_2017, Patrick_2009, and Duursma_2015 tended to lie closer to ETR_{max}, whereas Ellsworth_2004, Ethier & Livingston_2004, and Sharkey_2007 more often yielded lower J values; however, this ordering was not stable across crops and therefore cannot support a universal ranking. Because ETR_{max} is protocol dependent and affected by saturating PPFD setting, assumptions about absorptance and PSII partitioning, and leaf optical effects, it should be interpreted as an independent physiological consistency check rather than as a stand-alone accuracy benchmark (Evans, 2009; Yin *et al.*, 2009; Evans *et al.*, 2017; McClain & Sharkey, 2020).

The forward tests are more informative for downstream applications, because they assess whether fitted capacities transfer into a forward model with limited distortion. In our SCOPE-based simulation, Gregory_2021, Duursma_2015, Stinziano_2021, and often Sharkey_2007 remained closer to the empirical spread and showed relatively modest biases in both leaf-level and canopy-scale simulations. By contrast, Moualeu-Ngangue_2017 and Smith_2019 more often yielded higher and lower capacities, respectively, and showed the strongest positive and negative deviations. This ordering is model-dependent and may differ under other forward-model structures, because the forward tests reflect compatibility with a specific forward-model formulation rather than universal method accuracy (Rogers *et al.*, 2017b).

© 2026 The Author(s).
New Phytologist © 2026 New Phytologist Foundation.

The synthetic benchmark provides a further comparison under controlled assumptions. In this additional analysis, most methods recovered $V_{cmax,25}$ more closely than J_{25}, whereas J-related quantities were more often overestimated (Figs S19–S20). Duursma_2015 and Gregory_2021 were among the closest to the target $V_{cmax,25}$, while Ethier & Livingston_2004 underestimated $V_{cmax,25}$ but remained relatively close for J_{25}. Patrick_2009 and the Sharkey configurations showed larger positive departures. This benchmark is useful for assessing identifiability and bias potential, but because its outcome depends on the prescribed truth set and generating assumptions, it is better interpreted as a controlled test of retrieval behavior than as a definitive accuracy ranking (Sun *et al.*, 2014).

Taken together, these comparisons support application-dependent guidance rather than a universal ranking. Across the three evaluation lines, Gregory_2021 showed the clearest overall balance among external tools: It performed well in the forward-model transfer tests, recovered $V_{cmax,25}$ relatively well in the synthetic benchmark, and did not show the strongest ETR_{max} departures. This balance was not explained by any single assumption or label, such as full-curve fitting or Arrhenius-type $k(T)$, but likely arose from its combined implementation: full-curve nonlinear fitting, gas-exchange-based rather than fluorescence-constrained g_m estimation, nonlinear R_d estimation, and intermediate effective $V_{cmax,25}$ estimates. Duursma_2015 and Stinziano_2021 also showed useful transfer behavior, but require caution for R_d interpretation, and Duursma_2015 additionally produced high $J_{25}/V_{cmax,25}$ ratios when J-coordination is of interest. Sharkey_2007 and Sharkey_2016 were useful but conditional because of fixed C_i-threshold partitioning, with Sharkey_2016 additionally requiring matched A_n–Q data for J_{25}. Patrick_2009 remains valuable for uncertainty quantification, whereas Moualeu-Ngangue_2017 is better reserved for explicit g_m inference. For forward-model applications, partitioning should match the target model's A_c–A_j transition logic; for continuous co-limitation models such as SCOPE, fixed-threshold or low-C_i-only partitioning should be viewed as approximations.

Limitations and outlook

Our results should be interpreted in light of the finite set of crops, site years, and protocols used here. The relative importance of assumptions may differ under other species, stress conditions, or measurement designs. Our framework is therefore stronger in quantifying method-induced spread and transferability than in identifying a uniquely correct method, particularly because fully independent biochemical constraints on carboxylation capacity were unavailable. In addition, several parameters remain weakly identifiable from A_n–C_i data, creating equifinality among $V_{cmax,25}$, J_{25}, R_d, and g_m. Accordingly, the constrained $R_d = 0$ values used here should be viewed only as a fitting safeguard for estimating $V_{cmax,25}$ and J_{25}, not as respiration traits suitable for trait databases. The OAT and variance-based analyses captured main effects, but not nonlinear interactions. The forward tests isolated fitted $V_{cmax,25}$ within a single canopy framework, so they underrepresent parameter co-variation in real canopies and may differ under other radiative-transfer or stomatal-coupling schemes. Seasonal soybean $V_{cmax,25}$ was generated by interpolating between measurement dates, which may introduce additional temporal uncertainty.

These limitations highlight priorities for future work. Stronger evaluation will require coordinated datasets combining A_n–C_i curves with matched A_n–Q curves, replicated temperature steps, high-quality Chl fluorescence, and independent constraints on diffusion and carboxylation. Independent g_m checks, such as variable-J fluorescence or isotope-based diagnostics, are especially valuable for screening nonphysical solutions. On the modeling side, future work should move from point estimates to conditional inference, typically within Bayesian or model–data fusion frameworks that integrate priors, constraints, and multi-source observations to quantify uncertainty (Feng & Dietze, 2013). When raw curves or additional observations are unavailable, literature-derived values are better treated as uncertain priors and propagated forward; where independent observations exist (e.g. flux-based GPP, Chl, or leaf nitrogen), they can be updated through Bayesian calibration or data assimilation. $V_{cmax,25}$ can be modeled as a latent state within a state-space framework to generate trajectory ensembles and propagate temporal uncertainty. More broadly, progress requires reporting both fitted values and the configuration metadata used to derive them, enabling comparison, transfer, and validation under matched assumptions rather than as assumption-free traits.

Acknowledgements

This work was supported by the Natural Science Basic Research Program of Shaanxi Province (Youth, grant no. 2025JC-YBQN-237), the National Natural Science Foundation of China (grant no. 32501784), and the Research Start-up Fund of Northwest A&F University. The authors also acknowledge the Sanqin Scholars Smart Agriculture Innovation Team. Large language models were used only to assist with English language polishing and readability improvement. The authors carefully reviewed and edited all text after using these tools and take full responsibility for the final content of the manuscript.

Competing interests

None declared.

Author contributions

GW, CJ and QY designed the study; GW, ZY and YW collected the data. YW analyzed the data. YW and GW wrote the draft of the manuscript. YW, CL, CJ, CJB, GZ, NY, XF, QY and GW contributed to the interpretation of results and the text. All authors contributed revisions.

ORCID

Carl J. Bernacchi https://orcid.org/0000-0002-2397-425X
Xinyi Fan https://orcid.org/0009-0007-7054-9567

© 2026 The Author(s).
New Phytologist © 2026 New Phytologist Foundation.

14698137, 0, Downloaded from https://nph.onlinelibrary.wiley.com/doi/10.1111/nph.71358 by Northwest Agri & Forestry, Wiley Online Library on [14/06/2026]. See the Terms and Conditions (https://onlinelibrary.wiley.com/terms-and-conditions) on Wiley Online Library for rules of use; OA articles are governed by the applicable Creative Commons License

Chongya Jiang https://orcid.org/0000-0002-1660-7320
Yingnan Wei https://orcid.org/0009-0000-5632-2269
Genghong Wu https://orcid.org/0000-0002-6227-6390
Ning Yao https://orcid.org/0000-0002-5863-401X
Qiang Yu https://orcid.org/0000-0001-6950-1821

Data availability

The A_n–C_i measurement files used in this study and the Python scripts developed to calculate $V_{cmax,25}$ and J_{25} from these measurements are available at https://github.com/wyn-2024/photosynthesis.git. Publicly available fitting tools and model codes were used or called according to their original publications and documentation, as cited in the Materials and Methods section.

References

Bayat B, van der Tol C, Verhoef W. 2018. Integrating satellite optical and thermal infrared observations for improving daily ecosystem functioning estimations during a drought episode. *Remote Sensing of Environment* **209**: 375–394.

Bernacchi CJ, Singsaas EL, Pimentel C, Portis AR, Long SP. 2001. Improved temperature response functions for models of Rubisco-limited photosynthesis. *Plant, Cell & Environment* **24**: 253–259.

Bonan GB, Lawrence PJ, Oleson KW, Levis S, Jung M, Reichstein M, Lawrence DM, Swenson SC. 2011. Improving canopy processes in the Community Land Model version 4 (CLM4) using global flux fields empirically inferred from FLUXNET data. *Journal of Geophysical Research – Biogeosciences* **116**: G02014.

Brooks A, Farquhar GD. 1985. Effect of temperature on the CO_2/O_2 specificity of ribulose-1,5-bisphosphate carboxylase/oxygenase and the rate of respiration in the light: Estimates from gas-exchange measurements on spinach. *Planta* **165**: 397–406.

Buckley TN, Diaz-Espejo A. 2015. Reporting estimates of maximum potential electron transport rate. *New Phytologist* **205**: 14–17.

von Caemmerer S. 2000. Biochemical models of leaf photosynthesis. In: *Techniques in plant sciences no. 2*. Collingwood, Vic., Australia: CSIRO.

Campbell JE, Berry JA, Seibt U, Smith SJ, Montzka SA, Launois T, Belviso S, Bopp L, Laine M. 2017. Large historical growth in global terrestrial gross primary production. *Nature* **544**: 84–87.

Cano FJ, López R, Warren CR. 2014. Implications of the mesophyll conductance to CO_2 for photosynthesis and water-use efficiency during long-term water stress and recovery in two contrasting Eucalyptus species. *Plant, Cell & Environment* **37**: 2470–2490.

Chen RN, Liu XJ, Liu LY. 2025. Improved GPP upscaling from instantaneous measurements to daily sums using the light-use-efficiency-based model. *Agricultural and Forest Meteorology* **368**: 110529.

Collatz GJ, Ball JT, Grivet C, Berry JA. 1991. Physiological and environmental regulation of stomatal conductance, photosynthesis and transpiration: a model that includes a laminar boundary layer. *Agricultural and Forest Meteorology* **54**: 107–136.

Cottingham KL, Lennon JT, Brown BL. 2005. Knowing when to draw the line: designing more informative ecological experiments. *Frontiers in Ecology and the Environment* **3**: 145–152.

Croft H, Chen JM, Luo XZ, Bartlett P, Chen B, Staebler RM. 2017. Leaf chlorophyll content as a proxy for leaf photosynthetic capacity. *Global Change Biology* **23**: 3513–3524.

Dai H, Ye M, Walker AP, Chen XY. 2017. A new process sensitivity index to identify important system processes under process model and parametric uncertainty. *Water Resources Research* **53**: 3476–3490.

De Kauwe MG, Lin YS, Wright IJ, Medlyn BE, Crous KY, Ellsworth DS, Maire V, Prentice IC, Atkin OK, Rogers A *et al.* 2016. A test of the 'one-point method' for estimating maximum carboxylation capacity from field-measured, light-saturated photosynthesis. *New Phytologist* **210**: 1130–1144.

Detto M, Xu XT. 2020. Optimal leaf life strategies determine $V_{c,max}$ dynamic during ontogeny. *New Phytologist* **228**: 361–375.

van Diepen KHH, Goudriaan J, de Arellano JVG, de Boer HJ. 2022. Comparison of C_3 photosynthetic responses to light and CO_2 predicted by the leaf photosynthesis models of Farquhar et al. (1980) and Goudriaan et al. (1985). *Journal of Advances in Modeling Earth Systems* **14**: e2021MS002976.

Duursma RA. 2015. Plantecophys – an R package for analysing and modelling leaf gas exchange data. *PLoS ONE* **10**: e0143346.

Ellsworth DS, Reich PB, Naumburg ES, Koch GW, Kubiske ME, Smith SD. 2004. Photosynthesis, carboxylation and leaf nitrogen responses of 16 species to elevated pCO2 across four free-air CO_2 enrichment experiments in forest, grassland and desert. *Global Change Biology* **10**: 2121–2138.

Ethier GJ, Livingston NJ. 2004. On the need to incorporate sensitivity to CO2 transfer conductance into the Farquhar–von Caemmerer–Berry leaf photosynthesis model. *Plant, Cell & Environment* **27**: 137–153.

Evans JR. 2009. Potential errors in electron transport rates calculated from chlorophyll fluorescence as revealed by a multilayer leaf model. *Plant and Cell Physiology* **50**: 698–706.

Evans JR, Morgan PB, von Caemmerer S. 2017. Light quality affects chloroplast electron transport rates estimated from Chl fluorescence measurements. *Plant and Cell Physiology* **58**: 1652–1660.

Farquhar GD, von Caemmerer S, Berry JA. 1980. A biochemical model of photosynthetic CO_2 assimilation in leaves of C_3 species. *Planta* **149**: 78–90.

Feng XH, Dietze M. 2013. Scale dependence in the effects of leaf ecophysiological traits on photosynthesis: Bayesian parameterization of photosynthesis models. *New Phytologist* **200**: 1132–1144.

Gregory LM, McClain AM, Kramer DM, Pardo JD, Smith KE, Tessmer OL, Walker BJ, Ziccardi LG, Sharkey TD. 2021. The triose phosphate utilization limitation of photosynthetic rate: Out of global models but important for leaf models. *Plant, Cell & Environment* **44**: 3223–3226.

He LM, Chen JM, Liu JN, Zheng T, Wang R, Joiner J, Chou SR, Cheng B, Liu Y, Liu RG *et al.* 2019. Diverse photosynthetic capacity of global ecosystems mapped by satellite chlorophyll fluorescence measurements. *Remote Sensing of Environment* **232**: 111344.

Hu L, Montzka SA, Kaushik A, Andrews AE, Sweeney C, Miller J, Baker IT, Denning S, Campbell E, Shiga YP *et al.* 2021. COS-derived GPP relationships with temperature and light help explain high-latitude atmospheric CO_2 seasonal cycle amplification. *Proceedings of the National Academy of Sciences, USA* **118**: e2103423118.

Jiang CY, Ryu Y, Wang H, Keenan TF. 2020. An optimality-based model explains seasonal variation in C_3 plant photosynthetic capacity. *Global Change Biology* **26**: 6493–6510.

Kattge J, Knorr W. 2007. Temperature acclimation in a biochemical model of photosynthesis: a reanalysis of data from 36 species. *Plant, Cell & Environment* **30**: 1176–1190.

Keenan TF, Williams CA. 2018. The terrestrial carbon sink. *Annual Review of Environment and Resources* **43**: 219–243.

Kumarathunge DP, Medlyn BE, Drake JE, Rogers A, Tjoelker MG. 2019. No evidence for triose phosphate limitation of light-saturated leaf photosynthesis under current atmospheric CO_2 concentration. *Plant, Cell & Environment* **42**: 3241–3252.

Liu YH, Chen JM, He LM, Wang R, Smith NG, Keenan TF, Rogers C, Li WY, Leng JY. 2023. Global photosynthetic capacity of C_3 biomes retrieved from solar-induced chlorophyll fluorescence and leaf chlorophyll content. *Remote Sensing of Environment* **287**: 113457.

Lochocki EB, Salesse-Smith CE, McGrath JM. 2025. PHOTOGEA: an R package for closer fitting of photosynthetic gas exchange data with non-Gaussian confidence interval estimation. *Plant, Cell & Environment* **48**: 5104–5119.

Long SP, Bernacchi CJ. 2003. Gas exchange measurements, what can they tell us about the underlying limitations to photosynthesis? Procedures and sources of error. *Journal of Experimental Botany* **54**: 2393–2401.

Lu JS, Qi QM, Zheng GJ, Eitel JUH, Zhang QY, Zhang JY, Chen FD, Chen SM, Zhang F, Fang WM *et al.* 2025. Estimating photosynthetic traits in tea

© 2026 The Author(s).
New Phytologist © 2026 New Phytologist Foundation.

14698137, 0, Downloaded from https://nph.onlinelibrary.wiley.com/doi/10.1111/nph.71358 by Northwest Agri & Forestry, Wiley Online Library on [14/06/2026]. See the Terms and Conditions (https://onlinelibrary.wiley.com/terms-and-conditions) on Wiley Online Library for rules of use; OA articles are governed by the applicable Creative Commons License

chrysanthemum using high-throughput leaf hyperspectral reflectance. *Plant Physiology and Biochemistry* **221**: 109606.

Lu XH, Croft H, Chen JM, Luo YQ, Ju WM. 2022. Estimating photosynthetic capacity from optimized Rubisco-chlorophyll relationships among vegetation types and under global change. *Environmental Research Letters* **17**: 14028.

Luo XZ, Croft H, Chen JM, He LM, Keenan TF. 2019. Improved estimates of global terrestrial photosynthesis using information on leaf chlorophyll content. *Global Change Biology* **25**: 2499–2514.

McClain AM, Sharkey TD. 2020. Building a better equation for electron transport estimated from Chl fluorescence: accounting for nonphotosynthetic light absorption. *New Phytologist* **225**: 604–608.

Miller RG. 1986. *Beyond ANOVA: basics of applied statistics*. New York, NY, USA: Wiley Press.

Moualeu-Ngangue DP, Chen TW, Stutzel H. 2017. A new method to estimate photosynthetic parameters through net assimilation rate-intercellular space CO_2 concentration (A-C_i) curve and chlorophyll fluorescence measurements. *New Phytologist* **213**: 1543–1554.

Niinemets Ü, Díaz-Espejo A, Flexas J, Galmés J, Warren CR. 2009. Importance of mesophyll diffusion conductance in estimation of plant photosynthesis in the field. *Journal of Experimental Botany* **60**: 2271–2282.

Patrick LD, Ogle K, Tissue DT. 2009. A hierarchical Bayesian approach for estimation of photosynthetic parameters of C_3 plants. *Plant, Cell & Environment* **32**: 1695–1709.

Qian XJ, Liu LY, Chen XD, Zarco-Tejada P. 2021. Assessment of satellite chlorophyll-based leaf maximum carboxylation rate (V_{cmax}) using flux observations at crop and grass sites. *IEEE Journal of Selected Topics in Applied Earth Observations and Remote Sensing* **14**: 5352–5360.

Rogers A. 2014. The use and misuse of $V_{c,max}$ in Earth system models. *Photosynthesis Research* **119**: 15–29.

Rogers A, Kumarathunge DP, Lombardozzi DL, Medlyn BE, Serbin SP, Walker AP. 2021. Triose phosphate utilization limitation: an unnecessary complexity in terrestrial biosphere model representation of photosynthesis. *New Phytologist* **230**: 17–22.

Rogers A, Medlyn BE, Dukes JS, Bonan G, von Caemmerer S, Dietze MC, Kattge J, Leakey ADB, Mercado LM, Niinemets U *et al.* 2017a. A roadmap for improving the representation of photosynthesis in Earth system models. *New Phytologist* **213**: 22–42.

Rogers A, Serbin SP, Ely KS, Sloan VL, Wullschleger SD. 2017b. Terrestrial biosphere models underestimate photosynthetic capacity and CO_2 assimilation in the Arctic. *New Phytologist* **216**: 1090–1103.

Sexton T, Sankaran S, Cousins AB. 2021. Predicting photosynthetic capacity in tobacco using shortwave infrared spectral reflectance. *Journal of Experimental Botany* **72**: 4373–4383.

Sharkey TD. 2016. What gas exchange data can tell us about photosynthesis. *Plant, Cell & Environment* **39**: 1161–1163.

Sharkey TD, Bernacchi CJ, Farquhar GD, Singsaas EL. 2007. Fitting photosynthetic carbon dioxide response curves for C_3 leaves. *Plant, Cell & Environment* **30**: 1035–1040.

Smith NG, Keenan TF, Colin Prentice I, Wang H, Wright IJ, Niinemets Ü, Crous KY, Domingues TF, Guerrieri R, Ishida FY *et al.* 2019. Global photosynthetic capacity is optimized to the environment. *Ecology Letters* **22**: 506–517.

Stinziano JR, Roback C, Sargent D, Murphy BK, Hudson PJ, Muir CD. 2021. Principles of resilient coding for plant ecophysiologists. *AoB Plants* **13**: plab059.

Sun Y, Gu LH, Dickinson RE, Pallardy SG, Baker J, Cao YH, DaMatta FM, Dong XJ, Ellsworth D, Van Goethem D *et al.* 2014. Asymmetrical effects of mesophyll conductance on fundamental photosynthetic parameters and their relationships estimated from leaf gas exchange measurements. *Plant, Cell & Environment* **37**: 978–994.

van der Tol C, Verhoef W, Timmermans J, Verhoef A, Su Z. 2009. An integrated model of soil-canopy spectral radiances, photosynthesis, fluorescence, temperature and energy balance. *Biogeosciences* **6**: 3109–3129.

Walker AP, Hanson PJ, De Kauwe MG, Medlyn BE, Zaehle S, Asao S, Dietze M, Hickler T, Huntingford C, Iversen CM *et al.* 2014. Comprehensive ecosystem model-data synthesis using multiple data sets at two temperate forest free-air CO_2 enrichment experiments: Model performance at ambient CO_2 concentration. *Journal of Geophysical Research – Biogeosciences* **119**: 937–964.

Walker AP, Johnson AL, Rogers A, Anderson J, Bridges RA, Fisher RA, Lu D, Ricciuto DM, Serbin SP, Ye M. 2021. Multi-hypothesis comparison of Farquhar and Collatz photosynthesis models reveals the unexpected influence of empirical assumptions at leaf and global scales. *Global Change Biology* **27**: 804–822.

Walker AP, Quaife T, van Bodegom PM, De Kauwe MG, Keenan TF, Joiner J, Lomas MR, MacBean N, Xu CG, Yang XJ *et al.* 2017. The impact of alternative trait-scaling hypotheses for the maximum photosynthetic carboxylation rate (V_{cmax}) on global gross primary production. *New Phytologist* **215**: 1370–1386.

Wan L, Ma FD. 2024. Estimating leaf photosynthetic capacity using hyperspectral reflectance: model variability and transferability. *Computers and Electronics in Agriculture* **220**: 108837.

Wu GH, Jiang CY, Kimm H, Wang S, Bernacchi C, Moore CE, Suyker A, Yang X, Magney T, Frankenberg C *et al.* 2022. Difference in seasonal peak timing of soybean far-red SIF and GPP explained by canopy structure and chlorophyll content. *Remote Sensing of Environment* **279**: 113104.

Wu YF, Zhang ZY, Wu LS, Zhang YG. 2025. Solar-induced chlorophyll fluorescence and its relationship with photosynthesis during waterlogging in a maize field. *Agricultural and Forest Meteorology* **363**: 110404.

Wullschleger SD. 1993. Biochemical limitations to carbon assimilation in C_3 plants: a retrospective analysis of the A–Ci curves from 109 species. *Journal of Experimental Botany* **44**: 907–920.

Xu MZ, Chen JM, Liu YH, Wang R, Shang R, Leng JY, Shu L, Liu JE, Liu RG, Liu Y *et al.* 2024. Comparative assessment of leaf photosynthetic capacity datasets for estimating terrestrial gross primary productivity. *Science of the Total Environment* **926**: 171400.

Yang PQ, Prikaziuk E, Verhoef W, Van der Tol C. 2021. SCOPE 2.0: a model to simulate vegetated land surface fluxes and satellite signals. *Geoscientific Model Development* **14**: 4697–4712.

Ye ZP, Hu WH, Zhou SX, Robakowski P, Kang HJ, An T, Wang FB, Xiao YA, Yang XL. 2025. Limitations of the Farquhar-von Caemmerer-Berry Model in estimating the maximum electron transport rate: evidence from four C_3 species. *Biology-Basel* **14**: 630.

Yin XY, Struik PC. 2009. Theoretical reconsiderations when estimating the mesophyll conductance to CO_2 diffusion in leaves of C_3 plants by analysis of combined gas exchange and chlorophyll fluorescence measurements. *Plant, Cell & Environment* **32**: 1513–1524.

Yin XY, Struik PC, Romero P, Harbinson J, Evers JB, Van Der Putten PEL, Vos J. 2009. Using combined measurements of gas exchange and chlorophyll fluorescence to estimate parameters of a biochemical C_3 photosynthesis model: a critical appraisal and a new integrated approach applied to leaves in a wheat (*Triticum aestivum*) canopy. *Plant, Cell & Environment* **32**: 448–464.

Yu LY, Luo XZ, Croft H, Rogers CA, Chen JM. 2024. Seasonal variation in the relationship between leaf chlorophyll content and photosynthetic capacity. *Plant, Cell & Environment* **47**: 3953–3965.

Zheng Y, Shen RQ, Wang YW, Li XQ, Liu SG, Liang SL, Chen JM, Ju WM, Zhang L, Yuan WP. 2020. Improved estimate of global gross primary production for reproducing its long-term variation, 1982-2017. *Earth System Science Data* **12**: 2725–2746.

Supporting Information

Additional Supporting Information may be found online in the Supporting Information section at the end of the article.

Fig. S1 Comparison between $V_{cmax,25}$ and J_{25} for soybean in 2019 and 2020 calculated under with and without TPU conditions.

© 2026 The Author(s).
New Phytologist © 2026 New Phytologist Foundation.

14698137, 0, Downloaded from https://nph.onlinelibrary.wiley.com/doi/10.1111/nph.71358 by Northwest Agri & Forestry, Wiley Online Library on [14/06/2026]. See the Terms and Conditions (https://onlinelibrary.wiley.com/terms-and-conditions) on Wiley Online Library for rules of use; OA articles are governed by the applicable Creative Commons License

14698137, 0, Downloaded from https://nph.onlinelibrary.wiley.com/doi/10.1111/nph.71358 by Northwest Agri & Forestry, Wiley Online Library on [14/06/2026]. See the Terms and Conditions (https://onlinelibrary.wiley.com/terms-and-conditions) on Wiley Online Library for rules of use; OA articles are governed by the applicable Creative Commons License

Fig. S2 Comparison of $V_{cmax,25}$ and J_{25} values under configurations with and without TPU conditions for Perennial ryegrass, Red clover, Winter wheat (Yucheng), and Winter wheat (Yangling).

Fig. S3 Goodness-of-fit metrics (R^2 and RMSE) for fitted A_n–C_i curves for soybean across the 2019 and 2020 growing season (DOY 167–250) using different fitting methods.

Fig. S4 Goodness-of-fit metrics (R^2 and RMSE) for fitted A_n–C_i curves for Perennial ryegrass, Red clover, Winter wheat (Yucheng), and Winter wheat (Yangling) using different fitting methods.

Fig. S5 Comparison of $V_{cmax,25}$, J_{25}, and R_d for soybean in 2019 and 2020 calculated under $R_d < 0$ and $R_d = 0$ conditions.

Fig. S6 Comparison of $V_{cmax,25}$, J_{25}, and R_d for Perennial ryegrass, Red clover, Winter wheat (Yucheng), and Winter wheat (Yangling) calculated under $R_d < 0$ and $R_d = 0$ conditions.

Fig. S7 Seasonal dynamics of soybean photosynthetic capacity at measurement temperature derived from multiple A_n–C_i fitting configurations.

Fig. S8 Cross-species comparison of fitted photosynthetic capacity at measurement temperature using different A_n–C_i fitting configurations.

Fig. S9 Relationships between fitted J and fluorescence-derived ETR_{max} under different fitting configurations.

Fig. S10 Seasonal dynamics of soybean process-sensitive parameters in 2019 estimated under alternative process assumptions using the Sharkey_2007 baseline configuration.

Fig. S11 One-at-a-time sensitivity analysis of six process assumptions on fitted $V_{cmax,25}$ and J_{25} across perennial ryegrass, red clover, winter wheat (Yucheng), and winter wheat (Yangling).

Fig. S12 Cross-crop variation in R_d, g_m, and Γ^*_{25} estimated under alternative process assumptions using the Sharkey_2007 baseline configuration.

Fig. S13 One-at-a-time sensitivity analysis of discrete kinetic choices on fitted $V_{cmax,25}$ and J_{25} across perennial ryegrass, red clover, winter wheat (Yucheng), and winter wheat (Yangling).

Fig. S14 Observed and simulated A_n–C_i response curves under the parameter-matched scenario, in which $K_{c,25}$, $K_{o,25}$, and Γ^*_{25} used during fitting were harmonized to the SCOPE parameterization before refitting and forward simulation.

Fig. S15 Deviations between simulated assimilation rates and observed assimilation rates across the full A_n–C_i response curve under the parameter-matched scenario.

Fig. S16 Deviations between simulated assimilation rates and observed assimilation rates at $C_a = 400\ \mu mol\ mol^{-1}$ under the as-implemented scenario.

Fig. S17 Deviations between simulated assimilation rates and observed assimilation rates at $C_a = 400\ \mu mol\ mol^{-1}$ under the parameter-matched scenario.

Fig. S18 Effects of method-specific $V_{cmax,25}$ trajectories on soybean GPP simulated with SCOPE under the parameter-matched scenario in 2019.

Fig. S19 Synthetic benchmark of parameter recovery without matched K_c and K_o under controlled g_m and TPU configurations.

Fig. S20 Synthetic benchmark of parameter recovery with matched K_c and K_o under controlled g_m and TPU configurations.

Methods S1 A_n–C_i, A_n–Q, and Chl fluorescence measurement protocols.

Methods S2 SCOPE biochemical module settings used for forward simulations.

Methods S3 Synthetic benchmark design and inversion tests under controlled g_m and TPU configurations.

Table S1 Measurement settings for A_n–C_i and light-response curves of four crops across three field sites.

Table S2 Numbers of biological replicates for A_n–C_i curve measurements by crop, site year, and measurement date.

Table S3 Parameter values used in different equations and methods for photosynthetic model configurations.

Table S4 Method-specific retention rates of A_n–C_i curves after individual-curve quality control.

Table S5 Frequency of initially negative R_d estimates that were reset to zero by fitting method.

Table S6 Method-specific linear relationships between fitted J and fluorescence-derived ETR_{max} for soybean, other crops, and all crops.

Please note: Wiley is not responsible for the content or functionality of any Supporting Information supplied by the authors. Any queries (other than missing material) should be directed to the *New Phytologist* Central Office.

Disclaimer: The New Phytologist Foundation remains neutral with regard to jurisdictional claims in maps and in any institutional affiliations.

© 2026 The Author(s).
New Phytologist © 2026 New Phytologist Foundation.